LOW LOSS POLYMER NANOPARTICLE COMPOSITES FOR RF APPLICATIONS

Peter Kofinas
MARYLAND UNIV COLLEGE PARK

09/17/2014
Final Report

REPORT DOCUMENTATION PAGE

Form Approved
OMB No. 0704-0188

Public reporting burden for this collection of information is estimated to average 1 hour per response, including the time for reviewing instructions, searching existing data sources, gathering and maintaining the data needed, and completing and reviewing this collection of information. Send comments regarding this burden estimate or any other aspect of this collection of information, including suggestions for reducing this burden to Department of Defense, Washington Headquarters Services, Directorate for Information Operations and Reports (0704-0188), 1215 Jefferson Davis Highway, Suite 1204, Arlington, VA 22202-4302. Respondents should be aware that notwithstanding any other provision of law, no person shall be subject to any penalty for failing to comply with a collection of information if it does not display a currently valid OMB control number. **PLEASE DO NOT RETURN YOUR FORM TO THE ABOVE ADDRESS.**

1. REPORT DATE *(DD-MM-YYYY)* 11-08-2014	2. REPORT TYPE Final	3. DATES COVERED *(From - To)* 06/01/2009-08/30/2014

4. TITLE AND SUBTITLE

LOW LOSS POLYMER NANOPARTICLE COMPOSITES FOR RF APPLICATIONS

5a. CONTRACT NUMBER

5b. GRANT NUMBER
FA9550-09-1-0430

5c. PROGRAM ELEMENT NUMBER

6. AUTHOR(S)

Peter Kofinas
University of Maryland

5d. PROJECT NUMBER

5e. TASK NUMBER

5f. WORK UNIT NUMBER

7. PERFORMING ORGANIZATION NAME(S) AND ADDRESS(ES)

Air Force Office of Scientific Research

8. PERFORMING ORGANIZATION REPORT NUMBER

9. SPONSORING / MONITORING AGENCY NAME(S) AND ADDRESS(ES)

Charles Lee, Ph. D. AFOSR/RTD
charles.lee.21@us.af.mil
875 North Randolph Street
Suite 325, Room 3112

10. SPONSOR/MONITOR'S ACRONYM(S)

11. SPONSOR/MONITOR'S REPORT NUMBER(S)

12. DISTRIBUTION / AVAILABILITY STATEMENT

13. SUPPLEMENTARY NOTES

14. ABSTRACT

The aim of this project was the development of flexible magneto-dielectric polymer composites consisting of core-shell iron nanoparticles that possess high permeability (μ), high permittivity (ε) and minimal dielectric loss (tan δ). We have reported a novel method to obtain high permeability, low loss polymer composites with Fe/Ag core-shell nanoparticles. The noble metal (Ag) shell layer provides protection against oxidation of the Fe core yet, Fe/Ag nanoparticles cannot achieve high saturation magnetization (M_s). We optimized the synthesis of the Fe/Ag core-shell nanoparticles to suppress the formation of ferrous oxide, thus enhance μ and decreasing loss. Additionally, we have characterized the change in magnetic properties of the Fe/Ag core-shell nanoparticles during oxidation, to demonstrate the influence of oxidation on the M_s of the Fe/Ag core-shell nanoparticles. We also report a method to fabricate highly conductive strain-stable materials.

15. SUBJECT TERMS

Magnetodielectric, Radio Frequency, low loss

16. SECURITY CLASSIFICATION OF:			17. LIMITATION OF ABSTRACT	18. NUMBER OF PAGES	19a. NAME OF RESPONSIBLE PERSON Peter Kofinas
a. REPORT U	**b. ABSTRACT** U	**c. THIS PAGE** U	UU	1	**19b. TELEPHONE NUMBER** *(include area code)* (301) 4057335

Standard Form 298 (Rev. 8-98)
Prescribed by ANSI Std. Z39.18

Low Loss Polymer Nanoparticle Composites for RF Applications

Final Project Report

Grant# FA95500910430

PI: Peter Kofinas
University of Maryland

AFOSR Program Officer
Dr. Charles Y-C. Lee

1. Summary of Project

The aim of this project was the development of flexible magneto-dielectric polymer composites consisting of core-shell iron nanoparticles that possess high permeability (μ), high permittivity (ε) and minimal dielectric loss (tan δ). We have reported a novel method to obtain high permeability, low loss polymer composites with Fe/Ag core-shell nanoparticles. The noble metal (Ag) shell layer provides protection against oxidation of the Fe core yet, Fe/Ag nanoparticles cannot achieve high saturation magnetization (M_s).

We optimized the synthesis of the Fe/Ag core-shell nanoparticles to suppress the formation of ferrous oxide, thus enhance μ and decreasing loss. Additionally, we have characterized the change in magnetic properties of the Fe/Ag core-shell nanoparticles during oxidation, to demonstrate the influence of oxidation on the M_s of the Fe/Ag core-shell nanoparticles. The air-stable Fe/Ag core-shell nanoparticles were dispersed in an elastomer polymer matrix polydimethylsiloxane (PDMS) with 50wt% and 75wt% nanoparticle loading to form flexible polymer-nanoparticle composites.

We also report a method to fabricate highly conductive strain-stable materials. This fabrication process allows for conformal deposition on non-uniform substrates utilizing a combination of solution blow spinning and atomizing. The resulting stretchable conductor consists of an elastomeric fiber mat-silver nanoparticle composite. Initially, a fiber mat is blow spun from a solution of poly(styrene-block-isoprene-block-styrene) (SIS) elastomer in tetrahydrofuran (THF). To establish conductivity, a silver precursor solution is applied to a pre-spun mat and is nucleated into a network of silver nanoparticles, forming conductive pathways. The resulting composite achieves a uniform conductivity of 2000 S/cm at zero applied strain, with only a 12% increase in resistance after 400 cycles at 150% strain. The versatility of this approach was demonstrated by constructing various electronic devices including a stretchable light emitting diode (LED) circuit and a strain sensor on uniform and non-uniform substrates.

Archival Publications during reporting period:

"Sprayable Fiber Based Stretchable Conductors" M. Vural, A. M. Behrens, O. B. Ayyub, J. J. Ayoub, and P. Kofinas. ACS Nano, submitted 2014.

"Nanostructured Flexible Magneto-dielectrics for Radio Frequency Applications" M.Vural, B. Crowgey, L. Kempel, and P. Kofinas. Journal of Materials Chemistry C, 2, 756-763, 2014. DOI:10.1039/C3TC32113D.

"Surfactant-modified Nickel Zinc Iron Oxide / Polymer Nanocomposites for Radio Frequency Applications" T-I Yang, L. Kempel, and P. Kofinas. Journal of Nanoparticle Research, 12(8), 2967, 2010.
DOI: 10.1007/s11051-010-9887-4

2. Nanostructured Flexible Magneto-dielectrics for Radio Frequency

Abstract

Flexible magneto-dielectric composites were prepared by dispersing high saturation magnetization (M_s), low coercivity (H_c), air-stable, Fe/citrate nanoparticles and heterostructures of Fe/Ag core-shell nanoparticles in an elastomer (polydimethylsiloxane) matrix. Fe/citrate nanoparticles with a polycrystalline Fe core, a thin oxide layer, and a citrate shell have a M_s of 144 emu/g and H_c of 420 Oe. Fe/Ag core-shell nanoparticles exhibit lower M_s of 98 emu/g and H_c of 210 Oe prior to annealing. The saturation magnetization of Fe/Ag core-shell nanoparticles increased to 120 emu/g and the H_c decreased to 58 Oe after annealing, due to formation of the heterostructure and changes in the chemical composition and size of the oxide layer. Magneto-dielectric composites fabricated with air-stable Fe/citrate nanoparticles possess high μ (3.0) and moderate ε (11.6) while maintaining low magnetic (0.29) and dielectric (0.051) loss. Moreover magneto-dielectric composites fabricated using Fe/Ag heterostructures combine high μ (2.25) and ε (22.3) with low magnetic (0.24) and dielectric (0.09) loss. Radio Frequency antennas made from Fe/citrate nanoparticle and Fe/Ag heterostructure composites have achieved size reductions of 44% and 38%, respectively.

Introduction

Hybrid materials with high magnetic permeability (m) and dielectric permittivity (e) known as magneto-dielectric materials are essential for the development of high efficiency microwave electronic devices and their miniaturization.[1] Polymer-magnetic nanoparticle composites have promise as magneto-dielectric hybrids, due to their low magnetic and dielectric loss, mechanical flexibility, and ease of processability. The polymer matrix prevents particle aggregation, reducing conductivity losses, and provides mechanical flexibility. Magnetic nanoparticles dispersed in a polymer matrix contribute to the permeability and permittivity of the magneto-dielectric composite.[2]

The permeability of polymer-magnetic nanoparticle composites is limited by magnetic resonance frequency (f_{res}) and saturation magnetization (M_s) of the magnetic nanoparticles through the Snoek Limit.[3] The permeability drops significantly for frequencies above f_{res}. For this reason polymer composites containing MnZn and NiZn ferrites or similar materials with high permeability, yet low f_{res} have found limited application in microwave electronics.[4] Additionally, materials with low M_s such as iron oxides cannot achieve sufficient permeability to be utilized for microwave device miniaturization.[2, 5]

The dielectric and magnetic loss of magneto-dielectric composites are important properties that need to be minimized in order to improve the efficiency of microwave electronic devices. Dielectric losses mostly originate from eddy currents generated in the material. The eddy current generation in polymer-magnetic nanoparticle composites can be reduced by decreasing the size of nanoparticles below a critical dimension (skin depth).[6] It is possible to increase the skin depth of the hybrid material by decreasing the conductivity originating from the percolation of magnetic nanoparticles.[7] As a consequence low conductivity leads to low dielectric loss. The coercivity (H_c) of magnetic nanoparticles induces magnetic losses in polymer-magnetic nanoparticle composites.[8] Magnetic losses can be reduced without sacrificing any magnetization by the use of superparamagnetic nanoparticles. However, it is quite challenging to synthesize superparamagnetic nanoparticles with high M_s. Magnetic materials with high M_s such as ferromagnetic iron cannot maintain their magnetization at dimensions

smaller than the critical superparamagnetic size because of excessive oxidation.[9, 10] Polymer-magnetic nanoparticle composites reported in literature consist of either oxidized superparamagnetic nanoparticles with no coercivity and low M_s resulting in low μ, or high M_s ferromagnetic nanoparticles with substantial coercivity leading to high magnetic loss.[2, 5, 11, 12]

In this work, we report on the fabrication of two sets of flexible magneto-dielectric composites with low magnetic and dielectric loss. This is achieved by the dispersion of high M_s, low coercivity air-stable iron (Fe) nanoparticles and iron/silver (Fe/Ag) heterostructures in polydimethylsiloxane (PDMS) matrices. The magneto-dielectric composites made of air-stable Fe/citrate nanoparticles can be adapted to the fabrication of broadband RF antennas, since they possess high μ (3), while maintaining low magnetic (0.29) and dielectric (0.051) loss.[13] Additionally, Fe/citrate nanoparticle composites are shape compliant, allowing tensile elongation up to 15% strain before failure. Fe/Ag heterostructures formed by thermal annealing of Fe/Ag core-shell nanoparticles were dispersed in PDMS to fabricate magneto-dielectric composites with high μ (2.25) and ε (22.3), but low magnetic (0.24) and dielectric (0.09) loss, which makes them suitable for RF antenna miniaturization.[1, 14] The Fe/Ag heterostructure composites are able to deform plastically under tensile elongation up to 70% strain.

Experimental

Synthesis of air-stable Fe/citrate nanoparticles

Fe/citrate nanoparticles were synthesized at room temperature from $FeSO_4$ using $NaBH_4$ as the reducing agent. $FeSO_4 \cdot 7H_2O$ (10mmol) and trisodium citrate dihydrate (2mmol) were dissolved in 2.5 L deionized water. The mixture was stirred with a magnetic stirrer for 5 minutes, then $NaBH_4$ (20mmol) was added to the mixture to initiate nanoparticle nucleation. The mixture was allowed to react for 20 minutes, and the nanoparticles were extracted using a rare-earth magnet for sedimentation. The particles were washed with ethanol 10 times, then vacuum dried and stored at atmospheric conditions.

Synthesis of Fe/Ag core-shell nanoparticles and heterostructures

Fe/Ag core-shell nanoparticles were synthesized at room temperature using a similar method. In this procedure Fe/citrate nanoparticles were reacted for 5 minutes instead of 20 minutes, then an aqueous $AgNO_3$ (7ml, 0.5M) solution was injected into the reaction. The mixture was allowed to stir for 20 minutes, and the core-shell nanoparticles were collected using magnet sedimentation. The collected particles were washed with ethanol 10 times then vacuum dried. The Fe/Ag core-shell nanoparticles were annealed at 600°C under flow of reducing gas (Argon/Hydrogen (95%, 5%)) for 1 hour to form a heterostructure of Fe/Ag core-shell nanoparticle aggregates with a coherent interface. The resulting Fe/Ag heterostructures were kept under atmospheric conditions.

Preparation of flexible magneto-dielectric composites

PDMS (Sylgard 184, Dow Corning) was prepared by mixing base polymer with a curing agent in a 10:1 weight ratio. Fe/citrate nanoparticles or Fe/Ag heterostructures were mixed in the polymer at the desired nanoparticle loading. The polymer particle mixture was poured into a mold, placed in a vacuum dessicator for 30 minutes to remove air bubbles, and cured at 100°C for 4 hours.
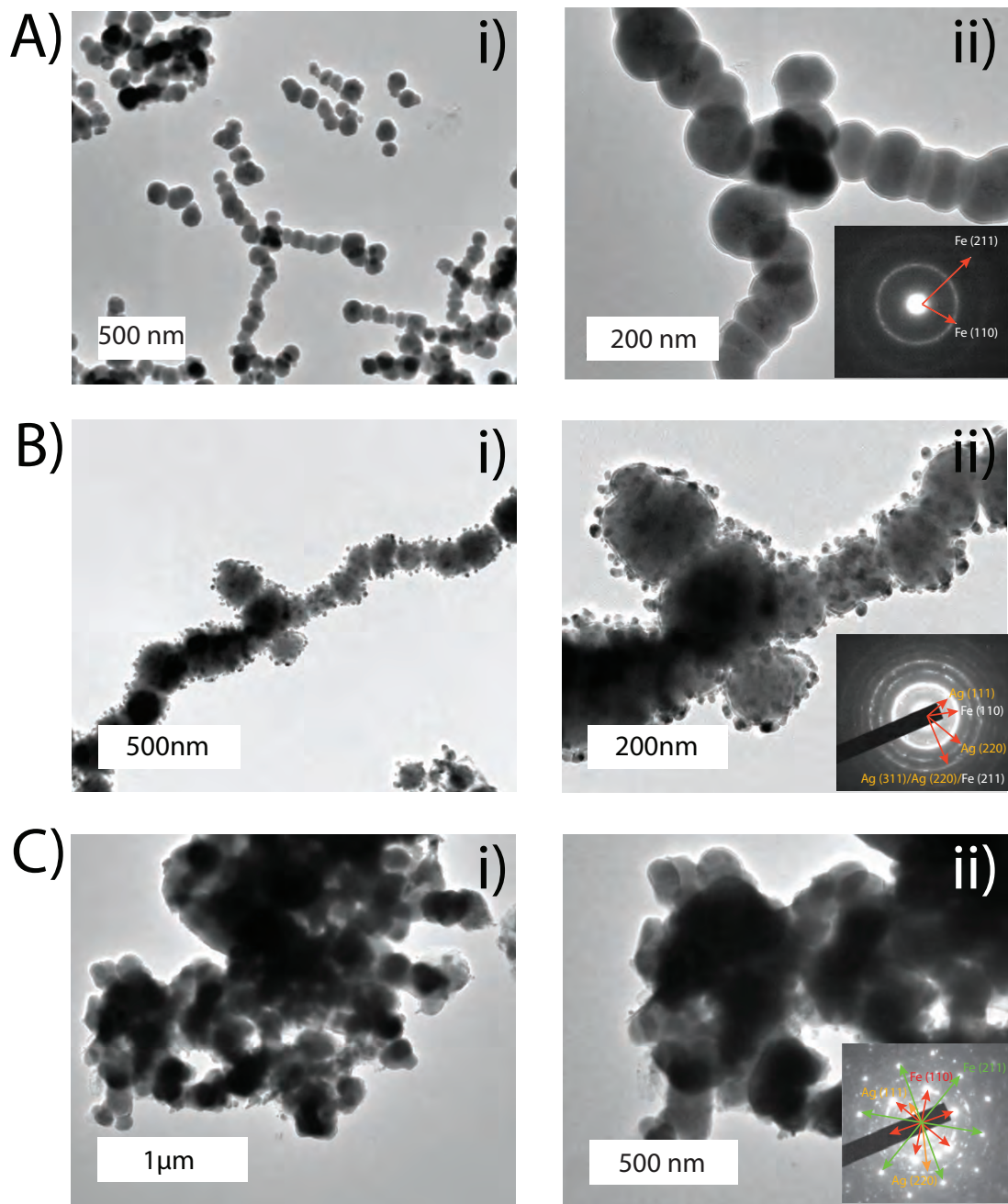
Fig. 1 TEM image of A) Fe/citrate nanoparticles, B) Fe/Ag core-shell nanoparticles, C) Fe/Ag heterostructures. The SAED characterization of each particle is placed as an inset.

Characterization

Transmission Electron Microscope (TEM) (JEOL 2100F), Powder X-Ray Diffraction (XRD)(Bruker C2 Discover-Source: Cu-Kα (λ=0.154nm)) and X-ray photoelectron spectrometer (Kratos Axis 165, Al Ka (1486.6 eV)) were used for structural and elemental characterization of the nanoparticles via imaging, Energy Dispersive X-Ray Spectroscopy (EDS), Selected Area Electron Diffraction (SAED), Powder Diffraction and X-ray Photoelectron Spectroscopy (XPS).

Vibrating Sample Magnetometer (VSM; Lakeshore 7400 series) was used to characterize the magnetic properties of the nanoparticles. Dynamic Mechanical Analysis (TA Instruments Q800) was used to characterize the mechanical properties of the polymer nanoparticle composites. The magnetodielectric properties of the composites were determined using an Agilent RF impedance/material analyzer (E4991A).

Results and Discussion

The TEM images and SAED patterns of air-stable Fe/citrate, Fe/Ag core-shell nanoparticles and Fe/Ag heterostructures are presented in Figure 1. The air-stable Fe/citrate nanoparticles capped with citrate developed a very thin oxide shell, which helps prevent further oxidation of the Fe core along with the citrate capping layer (Figure 1A). The average particle size for the air-stable Fe/citrate nanoparticles was measured to be 100 nm with a standard deviation of 19 nm (100 ± 19 nm). The Fe/Ag core-shell nanoparticles also have an oxide layer similar to the Fe/citrate nanoparticles, which separates the Fe core from the shell layer consisting of Ag nanoparticles (Figure 1B). The average diameter for the Fe/Ag core-shell nanoparticles was 120 ± 23 nm, which is slightly higher than the Fe/citrate nanoparticles because of the additional Ag nanoparticles covering the Fe core. The Fe/Ag heterostructures consist of aggregates of Fe/Ag core-shell nanoparticles with the Ag shell layer forming a coherent interface upon annealing at 600°C as illustrated in Figure 1C. In addition to TEM, SAED was used to identify the crystalline structure of each sample.
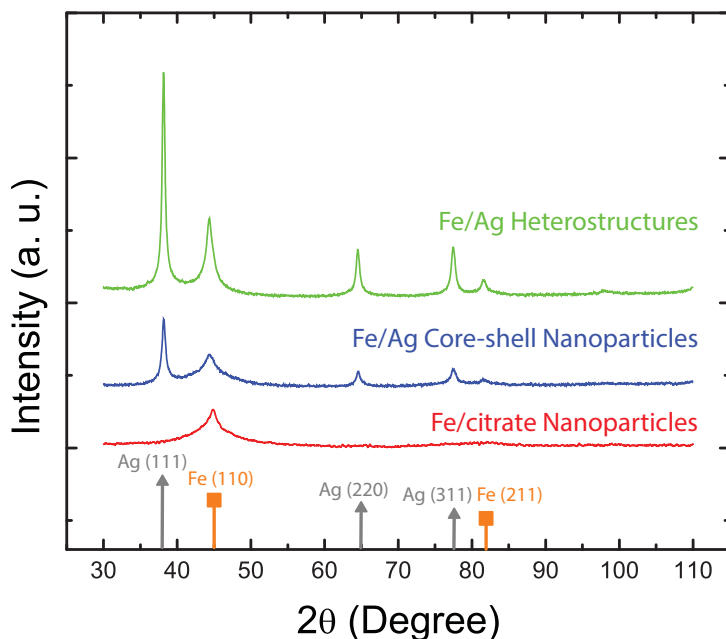

Fig. 2 Powder X-Ray Diffraction data of Fe/citrate nanoparticles, Fe/Ag core-shell nanoparticles and Fe/Ag heterostructures.

The SAED pattern of Fe/citrate nanoparticles indicates a microstructure of polycrystalline body centered cubic (bcc) Fe with Debye rings that correspond to, crystallographic planes Fe (110) and Fe (211) (Figure 1A(ii)-inset). The SAED pattern of Fe/Ag core-shell nanoparticles is an overlay of the polycrystalline bcc Fe pattern on the polycrystalline Ag pattern (Figure 1B(ii)-

inset). The Debye rings that represent the crystallographic planes in polycrystalline microstructure of Fe core and Ag shell are shown as an inset in Figure 1B(ii).

The crystalline structure of Fe/Ag core-shell nanoparticles changed significantly after thermal annealing under reducing gas flow. The crystal size of Ag shell increased after annealing, as inferred by the discontinuous Debye rings of Ag crystalline planes in the SAED pattern of the Fe/Ag heterostructure (Figure 1C(ii)-inset). The SAED pattern of the Fe/Ag heterostructure shows Laue diffraction patterns representing Fe crystalline planes instead of Debye rings. This indicates a significant increase in crystal size for the Fe core (Figure 1C(ii)-inset).

The average crystal size of Fe is an important structural parameter for the characterization and tunability of the magnetic properties (M_s, H_c) for both nanoparticles and heterostructures. Crystals below the critical superparamagnetic to ferromagnetic transition size of 10 nm for Fe result in zero coercivity.[15] However, further reducing the crystal size below the critical transition size leads to a decrease in M_s.[15] Powder X-Ray Diffraction (XRD) was utilized to identify the crystalline structure and crystal size of Fe in each material (Figure 2). The average crystal size of Fe in nanoparticles and heterostructures was determined from the diffraction peak of Fe (110) plane using Scherrer's Equation.[16] The XRD data indicates that the core of the nanoparticles consist of polycrystalline iron with an average crystal size of 5 nm for both Fe/citrate nanoparticles and Fe/Ag core-shell nanoparticles. Consistent with SAED patterns, the peaks of the Fe planes become sharper after annealing, which indicates an increase in crystal size. The average crystal size of Fe for the Fe/Ag heterostructures calculated from XRD data is 9.6 nm, which confirms the increase in crystal size with annealing (Figure 2).

The chemical composition of nanoparticles and heterostructures is equally important as the morphology for the displayed magnetic properties. Characterization of chemical composition for each nanoparticle and heterostructure was performed using localized EDS. XPS was used to characterize surface compositions of nanoparticles and heterostructures.

The STEM images and corresponding elemental EDS map for each nanoparticle and heterostructure are presented in Figure 3. The elemental EDS map of Fe/citrate nanoparticles shows a thin oxide layer covering the surface of the Fe core (Figure 3A). The oxide layer remains stable after being stored under ambient conditions at room temperature for 6 months (Figure S1-B). Upon annealing Fe/citrate nanoparticles with an analogous procedure for Fe/Ag core-shell nanoparticle annealing, the stable oxide layer grew thicker (Figure S1-B). The elemental EDS map of Fe/Ag core-shell shows a discontinuous shell layer formed by Ag nanoparticles around the Fe core prior to annealing (Figure 3B), consistent with the TEM images (Figure 1B). However, the EDS map does not indicate a distinct oxide shell (Figure 3B). After thermal annealing, the Fe/Ag core-shell nanoparticles form a heterostructure with an Ag shell with better coverage, as illustrated in the elemental EDS map (Figure 3C). The EDS map of the Fe/Ag heterostructure shows no obvious signs of oxidation at the surface. This can be attributed to the presence of a noble metal layer of Ag
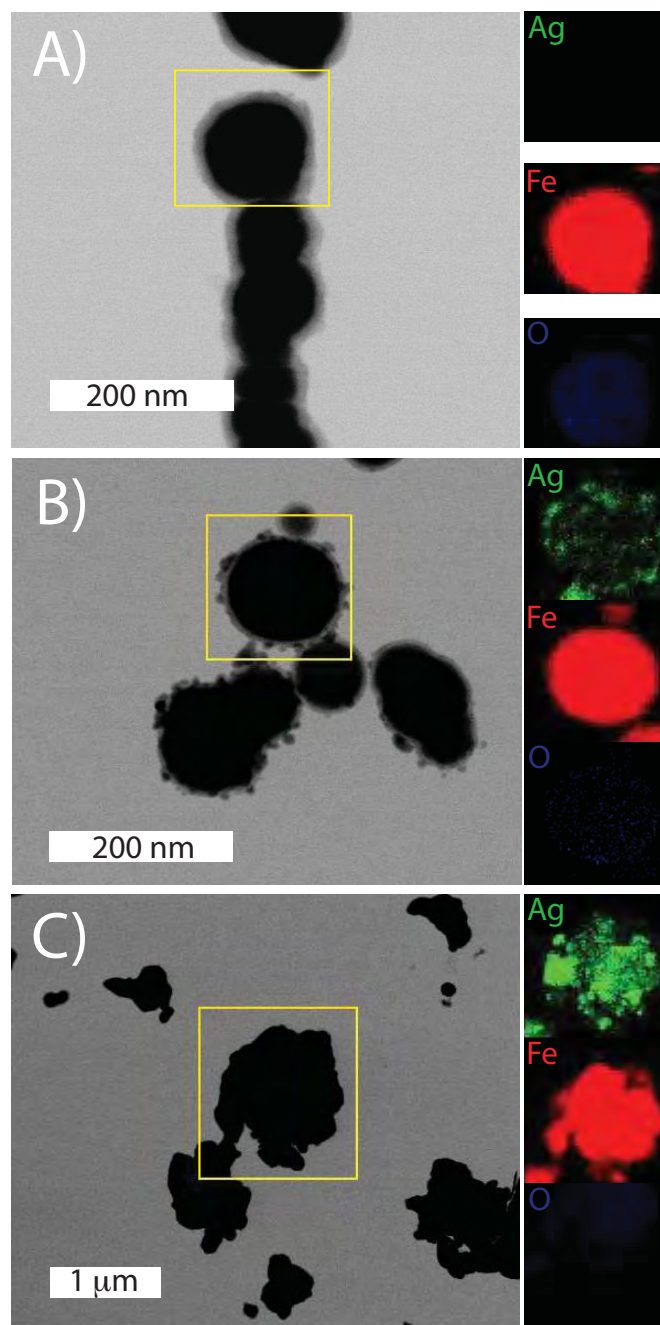.

Fig. 3 Scanning Transmission Electron Microscope (STEM) image and EDS elemental map of A) Fe/citrate nanoparticles, B) Fe/Ag core-shell nanoparticles, C) Fe/Ag heterostructures.
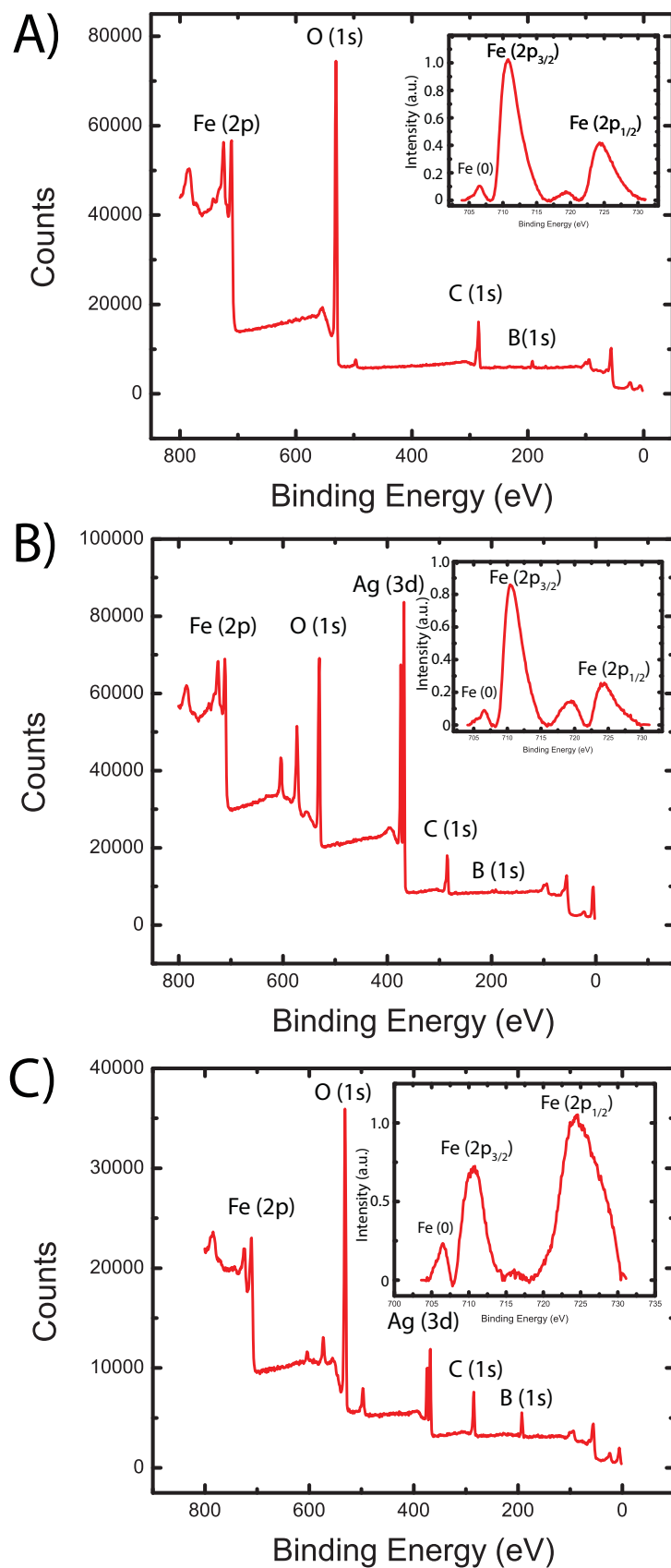
Fig. 4 XPS spectrum of A) Fe/citrate nanoparticle, B) Fe/Ag core-shell nanoparticle and Fe/Ag heterostructures. Localized XPS spectras around the Fe2p region is shown as an inset.
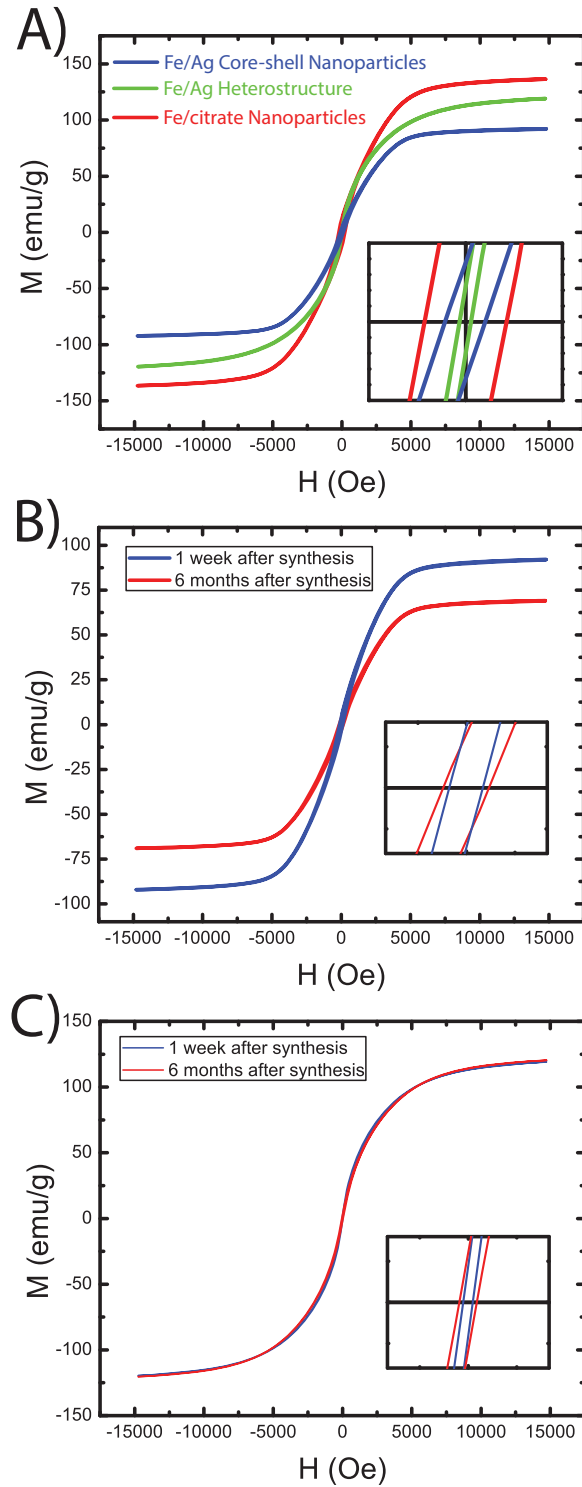
Fig. 5 A) Room temperature magnetic hysteresis curves for Fe/citrate nanoparticles, Fe/Ag core-shell nanoparticles and Fe/Ag heterostructures as synthesized. Time dependent magnetic hysteresis curves for B) Fe/Ag core-shell nanoparticles, and C) Fe/Ag heterostructures. The low-field magnetization curve is shown as an inset.

The characterization of the surface chemical composition of nanoparticles and heterostructures using XPS reveals the state of oxidation for Fe at the interface between the Fe core and shell layers (Figure 4). The XPS data agrees well with EDS for Fe/citrate nanoparticles where both indicate the existence of an oxide layer covering the Fe core (Figure 4A-inset). The oxide layer apparent at TEM images of Fe/Ag core-shell nanoparticles (Figure 1B) was confirmed by XPS (Figure 4B-inset). The oxide layer was identified as Fe_2O_3 from the satellite peak appearing at 718.8 eV for both Fe and Fe/Ag core-shell nanoparticles (Figure 4(A,B)).[17] The XPS data also indicates the existence of elemental Fe represented by the peak located at 706.7 eV (Figure 4(A, B)-inset). The existence of elemental Fe confirms that the oxide layer is as thin as the limited mean free path of X-rays.[18]

The XPS data of Fe/Ag heterostructures shows that the state of oxidation and thickness of the oxide layer has changed after annealing (Figure 4C). The oxide layer of Fe_2O_3 became Fe_3O_4 after annealing, which can be inferred by the absence of the satellite peak at 718.8 eV (Figure 4C-inset). Additionally, the elemental Fe peak became more prominent relative to the oxide related peaks ($Fe(3p_{1/2})$, $Fe(3p_{3/2})$), indicating that the oxide layer becomes thinner after annealing (Figure 4C-inset). The change in oxidation state and oxide layer thickness after annealing is consistent with previously reported Fe nanoparticles that were annealed in reducing ambient.[19]

The magnetic characterization correlates well with both the morphology and chemical composition of the nanoparticles and heterostructures. The Fe/citrate nanoparticles demonstrated significant M_s (144 emu/g), and high coercivity (420 Oe) (Figure 5A). The Fe/Ag core-shell nanoparticles have a lower M_s (98 emu/g) than the Fe/citrate nanoparticles, due to the non-magnetic shell layer of Ag.

The coercivity of Fe/Ag core-shell nanoparticles (210 Oe) is smaller than for Fe/citrate nanoparticles because the increase in size of the nanoparticle, reduces the influence of surface anisotropy.[20] The Fe/Ag heterostructures exhibit a higher M_s (120 emu/g) as compared to Fe/Ag core-shell nanoparticles (98 emu/g) due to the increase in average Fe crystal size and decrease in oxide layer thickness after annealing (Figure 5A).[11] The increase in Fe crystal size did not build additional coercivity because the average crystal size remained below the critical dimension for superparamagnetic to ferromagnetic transition. Moreover, the shape anisotropy became even less significant for Fe/Ag heterostructures since the size increased significantly as the Fe/Ag core-shell nanoparticles aggregate (Figure 1C). As a result, the coercivity of Fe/Ag heterostructures decreased to 58 Oe (Figure 5A). The magnetic properties of Fe/Ag core-shell nanoparticles and Fe/Ag heterostructures were evaluated after 6 months, in order to assess the stability of the nanoparticles (Figure 5(B-C)). The M_s of the Fe/Ag core-shell nanoparticle were decreased by 24% as a result of oxidation (Figure 5B), which was confirmed by EDS studies (Figure S2). The coercivity decreased slightly to 200 Oe. The magnetic properties of Fe/Ag heterostructures remained stable over the same period as a result of the protective Ag layer preventing oxidation (Figure 5C).

The Fe/citrate nanoparticles and Fe/Ag heterostructures were dispersed in a PDMS matrix and cured to form flexible magnetodielectric composites. The mechanical stress-strain curve for each polymer/nanoparticle composite is presented in Figure 6. The Young's modulus of Fe/citrate nanoparticle (1.75 MPa) and Fe/Ag heterostructure (0.79 MPa) composites with nanoparticle loading of 50wt% is higher than the modulus of the pure PDMS elastomer (0.56 MPa), indicating good adhesion between nanoparticles and the PDMS matrix (Figure 6A).[21] Both

Fe/citrate nanoparticles and Fe/Ag heterostructure composites with 50wt% nanoparticle loading exhibit 120% tensile elongation at break (Figure 6A). The composites made of Fe/citrate nanoparticles with 75wt% nanoparticle loading can deform elastically until failure at 15% strain (Figure 6B). On the other hand composites made of Fe/Ag heterostructure composites with 75wt% nanoparticle loading can deform plastically until failure at a strain of 70%, possibly due to better adhesion between Ag and PDMS (Figure 6B).[21] The Young's modulus of the composites increases with increasing nanoparticle loading; up to 11.1 MPa and 3.3 MPa for Fe/citrate nanoparticle and Fe/Ag heterostructure composites at 75wt% nanoparticle loading, respectively.
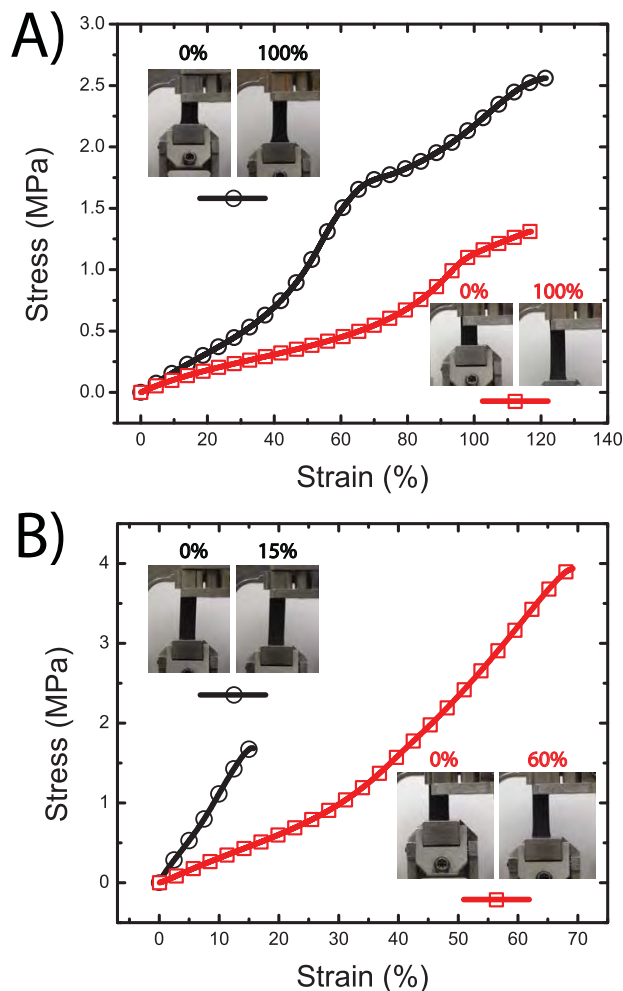

Fig. 6 Mechanical Stress/Strain curves for Fe/citrate (circles) and Fe/Ag (squares) heterostructure polymer composites with A) 50wt% and B) 75wt% nanoparticle loading. The images of elongated composites are shown as an inset.

The electromagnetic constants (m, e) and loss characteristics of both Fe/citrate nanoparticle and Fe/Ag heterostructure composites were measured at a frequency range of 1 MHz to 8 GHz. The ε dispersion relation for composites of Fe/citrate nanoparticles and Fe/Ag heterostructures with 50wt% nanoparticle loading was flat at this frequency range with no sign of dielectric resonance or relaxation that could lead to additional dielectric loss ($\tan d_e = e``/e`$) (Figure 7A). Due to the Ag shell, the ε values of Fe/Ag heterostructure composite (8) is higher than ε of the

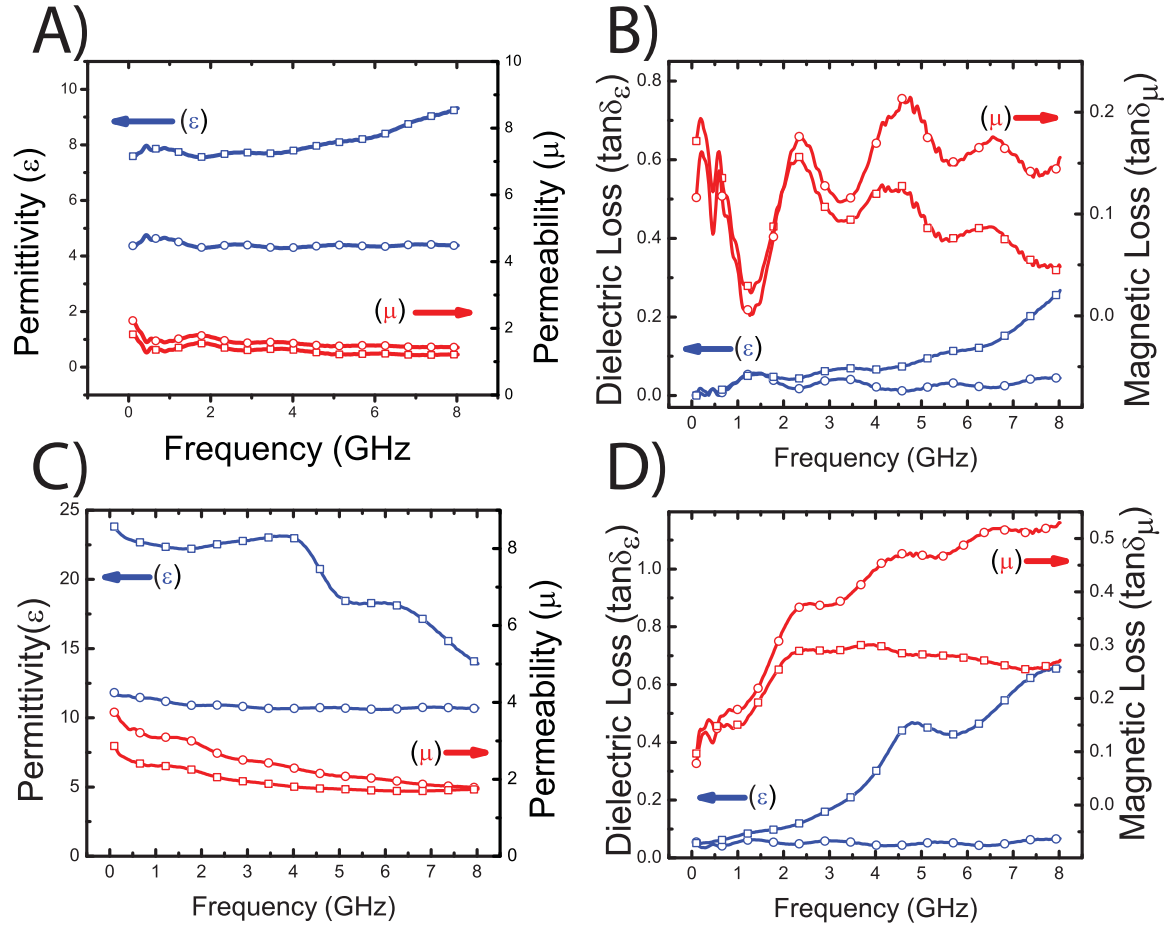Fe/citrate nanoparticle composite (4.2) with the same nanoparticle loading of 50wt%.

Fig. 7 A) Dielectric (ε), Magnetic Permeability (μ) dispersion and B) dielectric and magnetic loss values of Fe/citrate (circles) and Fe/Ag heterostructure (squares) composites with 50wt% nanoparticle loading. C) Dielectric (ε), Magnetic Permeability (μ) dispersion and D) dielectric and magnetic loss values of Fe/citrate (circles) and Fe/Ag heterostructure (squares) composites with 75wt% nanoparticle loading.

The dielectric loss values remain low up to a frequency of 3 GHz for both Fe/citrate nanoparticle (0.04) and Fe/Ag heterostructure (0.06) composites with nanoparticle loadings of 50wt% (Figure 7B). The dielectric loss value of Fe/Ag heterostructure composites increases drastically above 3 GHz due to conductivity losses introduced by the Ag shell. The μ and magnetic loss (tand$_m$=m``/m`) dispersion relation shows a magnetic relaxation starting at 2.25 GHz for the composites with 50wt% nanoparticle loading (Figure 7(A-B)). The μ values for both Fe/citrate nanoparticle and Fe/Ag heterostructure composites are promising for RF device fabrication, reaching 1.83 and 1.55 at 1.8 GHz, respectively (Figure 7A). The magnetic loss is significantly lower for Fe/citrate nanoparticle (0.06) composites and Fe/Ag heterostructure (0.07) composites at 1.8 GHz (Figure 7B). The magnetic loss increases more drastically for Fe/citrate nanoparticle composites at higher frequencies, which is possibly due to hysteresis losses and the influence of the Ag shell on magnetic relaxation by altering interparticle interactions (Figure 7B).[22]

The ε and dielectric loss values of the Fe/citrate nanoparticle composite with 75wt% nanoparticle loading are stable from 1 MHz to 8 GHz (Figure 7(C-D)). However, the ε and dielectric loss dispersion relation of the Fe/Ag heterostructure composite with 75wt% nanoparticle loading indicate a dielectric relaxation at 4.4 GHz, due to aggregation of the Fe/Ag heterostructure with increased concentration (Figure 7(C-D)).[23] As a result ε values decrease and the dielectric loss increases significantly for frequencies reaching 4.4 GHz. Even though the dielectric relaxation decreases ε and increases dielectric loss of the Fe/Ag heterostructure composites, they still possess high ε (22.3) and low dielectric loss (0.09) up to 3 GHz. The μ and magnetic loss dispersion relation of composites with 75wt% nanoparticle loading indicates a magnetic relaxation centered at 2.25 GHz similar to composites with 50wt% nanoparticle loading (Figure 7(C-D)). However, both Fe/citrate nanoparticle and Fe/Ag heterostructures have high μ and low magnetic loss values for frequencies lower than the magnetic relaxation frequency of 2.25 GHz. The Fe/citrate nanoparticle composites with 75wt% nanoparticle loading have μ and magnetic loss values of 3 and 0.29 at 1.8 GHz, respectively. The Fe/Ag heterostructure composites with 75wt% nanoparticle loading have a μ of 2.15 and magnetic loss of 0.24 at 1.8 GHz. The magnetic loss remains stable for frequencies beyond the magnetic relaxation for Fe/Ag heterostructure composites unlike Fe/citrate nanoparticle composites, which tend to have higher magnetic loss with increasing frequency (Figure 7D). As the particles get more densely packed with increasing concentration, the influence of the Ag shell as a spacer becomes more influential compared to coercivity effects, thus fixing the magnetic loss of Fe/Ag heterostructures at 0.24 beyond 2.25 GHz.[22] Flexible RF antennas have been fabricated using Fe/citrate nanoparticle and Fe/Ag heterostructure composites that operates at frequencies of 1.7 GHz and 1.9 GHz, respectively (Figure S3). The flexible magneto-dielectric composites fabricated using Fe/citrate nanoparticles reduced the size of the RF antenna operating at 1.7 GHz by 44%. The Fe/Ag heterostructure composite has scaled down the size of the RF antenna with an operation frequency of 1.9 GHz by 38%.

Elemental Analysis of Oxide Growth in Nanoparticles

Energy Dispersive X-ray Spectroscopy (EDS) of individual Fe/citrate and Fe/Ag core–shell nanoparticles was used to evaluate possible oxide layer growth. The oxidation characteristics of Fe nanoparticles with a citrate shell were investigated by exposing thermally annealed and non-annealed samples to ambient atmosphere at room temperature for 6 months. The EDS analysis shows that the non-annealed Fe nanoparticles are resistant to oxidation with their citrate shell remaining intact (Figure S1-A). However, the annealed Fe nanoparticles develop an oxide shell in the absence of the citrate shell over this time period. (Figure S1-B).
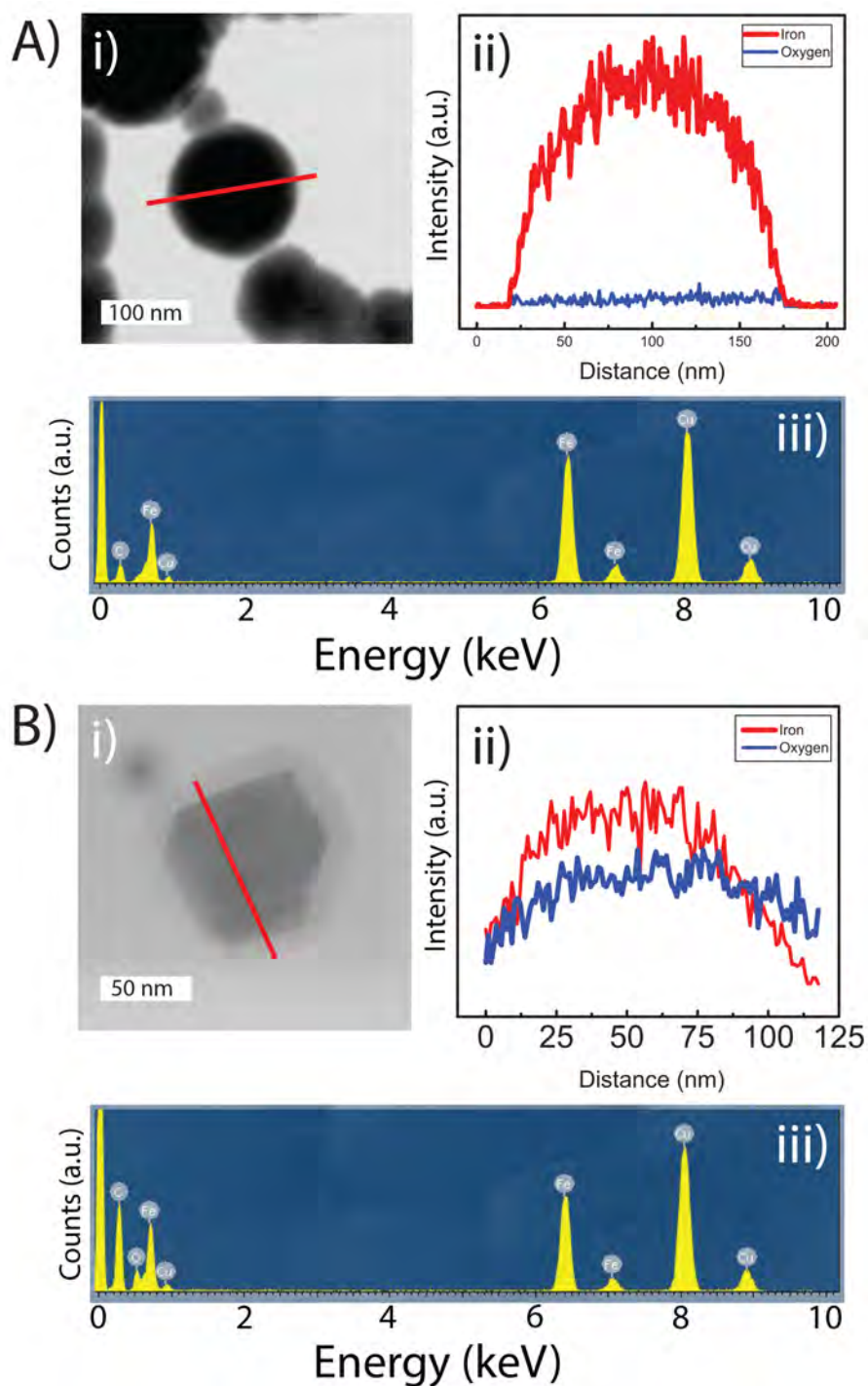
Figure S1. A) Scanning Transmission Electron Microscope (STEM) image (i), EDS elemental line scan (ii), EDS energy spectrum (iii) of non-annealed Fe/citrate nanoparticle. B) Scanning Transmission Electron Microscope (STEM) image (i), EDS elemental line scan (ii), EDS energy spectrum (iii) of annealed Fe/citrate nanoparticle.

EDS analysis also reveals that thermal annealing aids in preventing oxidation of Fe/Ag core-shell nanoparticles. The Fe/Ag core-shell nanoparticles remain unoxidized up to a week prior to thermal annealing (Figure S2-A). However, the discontinuous Ag shell layer of the Fe/Ag core-shell nanoparticles allows slow oxidation of the Fe core (Figure S2-B). As a result of slow oxidation, the oxide formation is detectable for core-shell nanoparticles that are not annealed and kept in ambient atmosphere for 6 months (Figure S2-B). Thermally annealed Fe/Ag core-shell nanoparticles that forms the Fe/Ag heterostructures show no further oxidation after 6 months (Figure S2-C). Thermal annealing leads to a thicker and continuous Ag shell that provides better protection against oxidation.
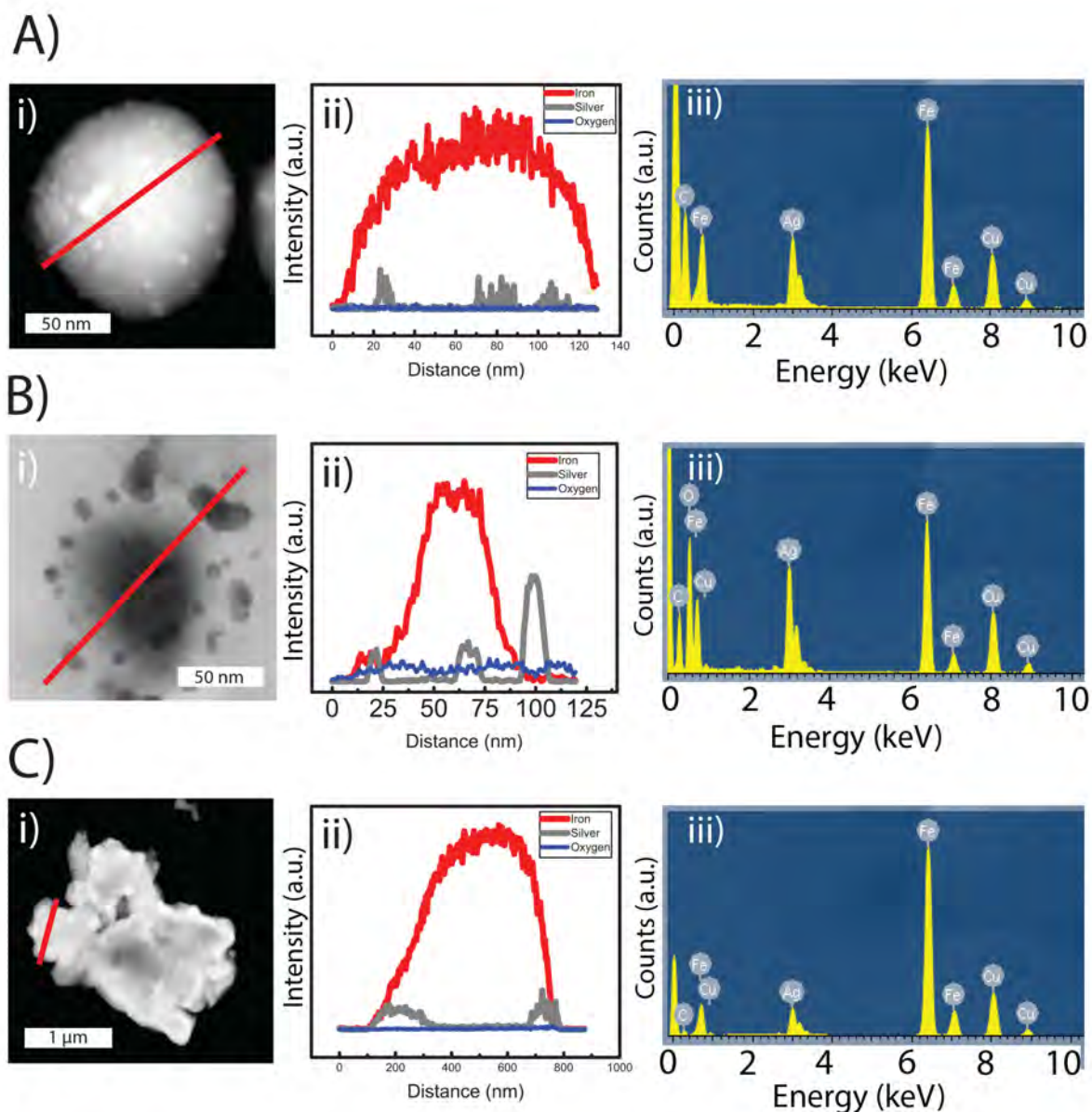

Figure S2. A) Scanning Transmission Electron Microscope (STEM) image (i), EDS elemental line scan (ii), EDS energy spectrum (iii) of Fe/Ag core shell nanoparticle (1 week after synthesis). B) Scanning Transmission Electron Microscope (STEM) image (i), EDS elemental line scan (ii), EDS energy spectrum (iii) of Fe/Ag core-shell nanoparticle (6 months after synthesis). C) Scanning Transmission Electron Microscope (STEM) image (i), EDS elemental line scan (ii), EDS energy spectrum (iii) of Fe/Ag heterostructures (6 months post synthesis).

16

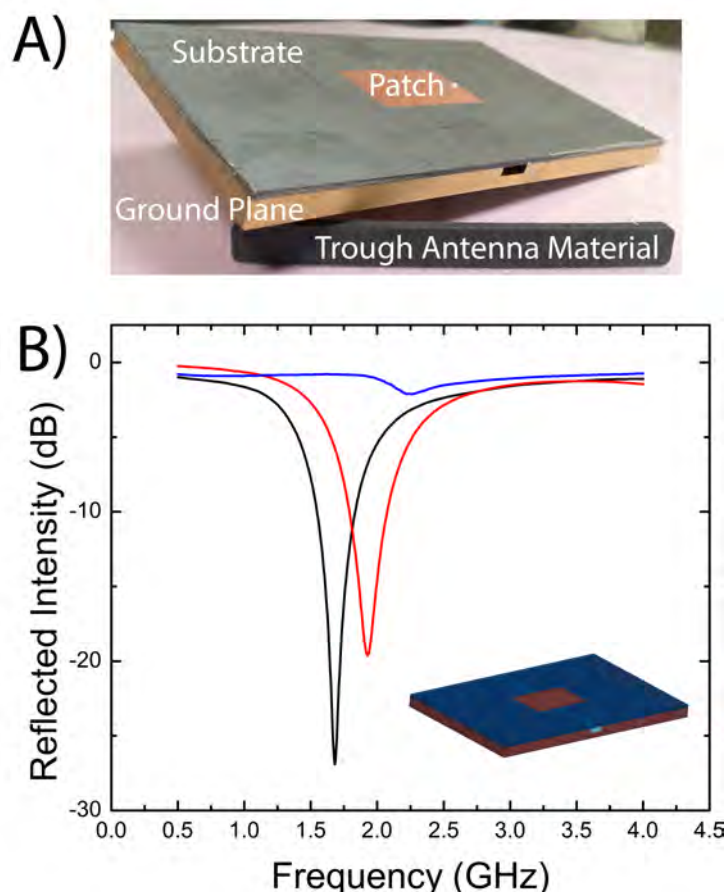**Embedded-Trough Patch Radio Frequency Antennas**

Figure S3. A) Image of embedded trough radio frequency antenna assembly. B) Reflected electromagnetic intensity spectrum for RF antennas with air filled trough (blue), Fe/citrate nanoparticle composite filled trough (black) and Fe/Ag heterostructure composite filled trough (red).

The device performance of flexible magneto-dielectric composites was tested by fabricating embedded-trough patch antennas with Fe/citrate nanoparticle and Fe/Ag heterostructure composites (75wt% nanoparticle loading). The flexible magneto-dielectric composites were placed in the trough of a patch antenna as illustrated in Figure S3-A and the reflected intensity spectrum was measured (Figure S3-C). The RF patch antenna with the Fe/citrate nanoparticle composite placed in the trough has a bandwidth of 12% at -10 dB. The bandwidth of the RF patch antenna with the Fe/Ag heterostructure composite was measured as 9.6% at -10 dB. The slightly higher bandwidth demonstrated by the Fe/citrate nanoparticle composite could be attributed to a higher m/e ratio. The RF antennas exhibit resonance at 1.7 GHz for the Fe/citrate nanoparticle composite trough and 1.9 GHz for the Fe/Ag heterostructure composite trough. The resultant size reduction percentages, as calculated from the resonance frequencies of equal length troughs, are 44% for the Fe/citrate nanoparticle composite and 38% for the Fe/Ag heterostructure composite.

Conclusions

We have fabricated elastic magneto-dielectric composites with low loss by embedding high M_s, low H_c, air-stable magnetic nanoparticles and heterostructures in an elastomer matrix (PDMS). Fe/citrate nanoparticles and Fe/Ag heterostructures have demonstrated good adhesion with the PDMS matrix. As a result the composites with 50wt% nanoparticle loading remain flexible up to a tensile elongation of 120%. These composites demonstrated promising ε and μ values with low dielectric and magnetic loss, while still maintaining their flexibility. The utilization of magnetic nanoparticles with appropriate crystal size, while still protecting the magnetic core against oxidation, provide a substantial advantage regarding ε, μ, loss values, and tunability of material properties for various applications in the field of RF communication devices. The Fe/citrate nanoparticle composites demonstrated higher permeability and lower dielectric loss due to the absence of a highly conductive and non-magnetic Ag layer. Conversely, the Ag layer allowed Fe/Ag heterostructure composites to achieve higher permittivity, lower magnetic loss and better mechanical elasticity. The composites have reduced the size of RF patch antennas as much as 44%. We believe this simple, yet effective method for designing and processing magneto-dielectric materials with different functionalities can have application in the construction of various communication devices for flexible RF electronics.

References

1.   A. O. Karilainen, P. M. T. Ikonen, C. R. Simovski and S. A. Tretyakov, *Ieee T Antenn Propag*, 2011, 59, 3991-3998.
2.   T. I. Yang, R. N. C. Brown, L. C. Kempel and P. Kofinas, *J Magn Magn Mater*, 2008, 320, 2714-2720.
3.   J. L. Snoek, *Physica*, 1948, 14, 207-217.
4.   B. D. Cullity and C. D. Graham, *Introduction to Magnetic Materials*, Hoboken: Wiley, 2009.
5.   A. Caprile, M. Coisson, F. Fiorillo, P. Kabos, O. M. Manu, E. S. Olivetti, M. A. Olariu, M. Pasquale and V. A. Scarlatache, *Ieee T Magn*, 2012, 48, 3394-3397.
6.   L. Z. Wu, J. Ding, H. B. Jiang, L. F. Chen and C. K. Ong, *J Magn Magn Mater*, 2005, 285, 233-239.
7.   Y. Shirakata, N. Hidaka, M. Ishitsuka, A. Teramoto and T. Ohmi, *Ieee T Magn*, 2008, 44, 2100-2106.
8.   C. Morales, J. Dewdney, S. Pal, S. Skidmore, K. Stojak, H. Srikanth, T. Weller and J. Wang, *Ieee T Microw Theory*, 2011, 59, 302-310.
9.   F. Dumestre, B. Chaudret, C. Amiens, P. Renaud and P. Fejes, *Science*, 2004, 303, 821-823.
10.   L. M. Lacroix, S. Lachaize, A. Falqui, M. Respaud and B. Chaudret, *J Am Chem Soc*, 2009, 131, 549-557.
11.   T. I. Yang, R. N. C. Brown, L. CKempel and P. Kofinas, *Nanotechnology*, 2011, 22.
12.   T. I. Yang, R. N. C. Brown, L. C. Kempel and P. Kofinas, *J Nanopart Res*, 2010, 12, 2967-2978.
13.   S. Borah and N. S. Bhattacharyya, *Compos Part B-Eng*, 2012, 43, 1988-1994.
14.   L. Yang, L. J. Martin, D. Staiculescu, C. P. Wong and M. M. Tentzeris, *Ieee T Microw Theory*, 2008, 56, 3223-3230.
15.   D. L. Huber, *Small*, 2005, 1, 482-501.
16.   Z. Zhang, F. Zhou and E. J. Lavernia, *Metall Mater Trans A*, 2003, 34A, 1349-1355.
17.   H. S. Lim, J. W. Oh, S. Y. Kim, M. J. Yoo, S. D. Park and W. S. Lee, *Chem Mater*, 2013, 25, 3315-3319.
18.   D. D. Sarma, P. K. Santra, S. Mukherjee and A. Nag, *Chem Mater*, 2013, 25, 1222-1232.
19.   S. H. Sun and H. Zeng, *J Am Chem Soc*, 2002, 124, 8204-8205.
20.   C. R. Vestal and Z. J. Zhang, *Nano Lett*, 2003, 3, 1739-1743.
21.   A. Goyal, A. Kumar, P. K. Patra, S. Mahendra, S. Tabatabaei, P. J. J. Alvarez, G. John and P. M. Ajayan, *Macromol Rapid Comm*, 2009, 30, 1116-1122.
22.   N. A. Frey, M. H. Phan, H. Srikanth, S. Srinath, C. Wang and S. Sun, *J Appl Phys*, 2009, 105.
23.   Y. Shen, Y. H. Lin and C. W. Nan, *Adv Funct Mater*, 2007, 17, 2405-2410.

3. Sprayable Elastomeric Fiber Based Stretchable Conductors

Stretchable conductor research has expanded significantly due to interest in mechanically deformable circuitry for use in flexible electronics. Such materials have applications in stretchable displays,[1] solar cells,[2] field effect transistors,[3] radio frequency antennas,[4] strain and tactility sensors,[5, 6] and epidermal electronics.[7, 8] Current approaches use assemblies of conductive and elastomeric components to develop materials that maintain electrical properties under strain. However, the mechanical properties of the conductive component introduce a compromise between elasticity and electrical conductivity.[9]

State of the art stretchable conductors have been demonstrated using networks of nanowires or nanotubes back-filled with elastomers,[10-12] polymer-nanoparticle composites,[13, 14] liquid metal filled microfluidic channels,[4, 15] conductive networks on pre-strained or buckled substrates,[16] and metallic fractal or microwire patterns on polymer substrates.[7, 17] Metallic nanowire and carbon nanotube based materials have shown mechanical and electrical robustness under cyclic deformation.[11, 12] However, when these systems reach high conductivities there is a reduction in maximum tensile strain due to increased rigid filler content.[12, 18] Polymer-nanoparticle composites have achieved enhanced mechanical elasticity in highly conductive systems but have high percolation thresholds when nanoparticles are dispersed within the polymer matrix.[13] Liquid metal-based elastic conductors compromise the overall material strength due to the inherent mechanically poor nature of the conductive component. Metallic patterns are able to maintain the bulk electrical properties of the conductive component under strain, though there are defined limitations for the ultimate achievable strain values.[7]

Another important consideration in the development of elastic conductors is the ease of fabrication and deposition of the material onto non-uniform substrates. This is especially important for applications such as epidermal electronics[7] and smart textiles.[19] Current methodologies utilize complex lithographical methods,[20] printing,[21] or spray techniques,[6] and require subsequent transfer from a planar fabrication substrate to a non-uniform substrate of interest. During this process, the resulting mechanical deformation causes degradation of the electrical properties of the material.[22] To our knowledge direct deposition of stretchable conductors on non-uniform substrates has not yet been demonstrated.

Here we report a method to fabricate highly conductive strain-stable materials. This fabrication process allows for conformal deposition on non-uniform substrates utilizing a combination of solution blow spinning[23] and atomizing. The resulting stretchable conductor consists of an elastomeric fiber mat-silver nanoparticle composite. Initially, a fiber mat is blow spun from a solution of poly(styrene-block-isoprene-block-styrene) (SIS) elastomer in tetrahydrofuran (THF) (Figure 1). To establish conductivity, a silver precursor solution is applied to a pre-spun mat and is nucleated into a network of silver nanoparticles, forming conductive pathways. The resulting composite achieves a uniform conductivity of 2000 S/cm at zero applied strain, with only a 12% increase in resistance after 400 cycles at 150% strain. The versatility of this approach was demonstrated by constructing various electronic devices including a stretchable light emitting diode (LED) circuit and a strain sensor on uniform and non-uniform substrates.

We initially investigated the solution and deposition conditions that produce optimal fiber networks. A network structure consisting of high aspect ratio cylindrical fibers is beneficial for homogeneous nanoparticle distribution and conductive pathway formation. Microstructure characterization revealed that a fiber network structure was achieved for SIS/THF solutions with

a concentration of 20% (wt/vol) (Figure 2a). The average diameter of elastomeric fibers after spinning was 1.66 mm. The fiber mats were swollen in silver nanoparticle precursor solution containing various concentrations of silver trifluoroacetate (STFA) in ethanol. Through this process the fiber diameter increased to an average of 3.28 mm and fiber-to-fiber contact was enhanced, resulting in the formation of fiber bundles (Figure 2b). Hydrazine hydrate solution was then used to reduce the silver ions in the precursor-swollen mats. Individual fiber diameter decreased in comparison to the swollen state, however, bundles consisting of multiple fibers persisted after nanoparticle nucleation (Figure 2c). Transmission electron microscopy (TEM) of the resulting silver nanoparticle-polymer fiber composite cross-section revealed that the nanoparticles populate the outer surface (Figure 2c-inset). Upon stretching, fibers orient in the direction of applied strain (Figure 2d). Fiber bundles were still present after stretching to 100% strain for conductors fabricated with 25% (wt/vol) STFA solutions (Figure 2d-inset). This is in contrast to composites fabricated with lower STFA solution concentrations, in which bundles break up into individual fibers during stretching (Figure S1). This indicates that increased silver nanoparticle content provides additional stability for already present fiber-to-fiber contacts.

The nanoparticle precursor solution concentration effect on conductivity was assessed by measuring bulk conductivity of the polymer-nanoparticle composites (Figure 3a). Maximum conductivity values (2000 S/cm) were achieved with a precursor concentration range between 25% and 35% (wt/vol). Fabrication of composites with 30% and 35% (wt/vol) STFA solutions led to an increased variability in conductivity that can be attributed to fiber mat delamination during nucleation. This is further reflected in elastic recovery experiments, where these materials yielded before completing cycling up to 150% strain (Figure S3).

Electrical properties under cyclic strain were characterized for conductive composites. Precursor concentration greatly influenced the strain dependence of electrical properties. The normalized resistance (R/R_0) values of polymer-nanoparticle composites reach 1.85 at 150% strain (10% (wt/vol) STFA) with appreciable hysteresis (Figure 3b). When STFA concentration is increased to 25% (wt/vol) normalized resistance at 150% strain decreases to 1.06 with a significant reduction in hysteresis after a single cycle (Figure 3b). This strain-stable electrical behavior was additionally observed by a minimal resistance increase after 400 cycles at 150% strain (R/R_0=1.13), a value that stabilized after the 300th cycle (Figure 3c,d). State of the art stretchable elastic conductors with similar and higher bulk conductivity have not achieved comparable stability of electrical properties under mechanical deformation ((R/R_0=10, s_0=2000 S/cm, 150% strain),[24] ($R/R_0 \approx$4.6, s_0=11000 S/cm, 110% strain),[13] (R/R_0=7, s_0=5200 S/cm, 140% strain)[14]).

We believe these unique electromechanical characteristics are majorly the result of bound fiber-to-fiber connections, originating from silver nanoparticle reinforced fiber bundles (Figure 2c,d). Bound fiber-to-fiber connections are known to contribute significantly to mechanical strength of elastomeric fiber mats.[25] To investigate the influence of these structures on the overall composite's mechanical properties, energy dissipation (Figure 3f,S4) was calculated from cyclic stress/strain curves (Figure 3e). This analysis revealed that dissipative losses at low strains (below ~25% strain) stem from the rearrangement of unbound fibers. As strain values increase (above ~25% strain) dissipative losses are compounded by the failure of bound fiber-to-fiber junctions. This transition, the intersection between two distinct linear correlations relating energy dissipation to strain (Figure 3f), is in agreement with the onset of both plastic deformation and hysteresis in electrical properties (Figure 3b,c,e).

A proof of concept device utilizing this approach on a non-uniform substrate was demonstrated by depositing and patterning strain sensors on nitrile gloves. The elastomeric fiber mat was first solution blow spun directly on a nitrile glove (Figure 4a). A solution pen (Paasche F-I/32) with adjustable flow rate was then used to deposit a line of precursor solution (25% (wt/vol)) along each finger. The patterned lines were then nucleated into silver nanoparticles, thereby forming stretchable conductive lines corresponding to each finger. Resistance of each conductive line was measured while performing multiple hand gestures, where normalized resistance values corresponded to individual finger movements (Figure 4a).

The strain dependence of electrical properties was evaluated separately to identify the difference between patterned stretchable conductors and bulk stretchable conductors (Figure S5). Additionally, we constructed a basic circuit consisting of 2 LEDs connected with a stretchable conductor prepared using 25% (wt/vol) STFA solution (Figure 4b). The illumination of both LEDs remained stable while the conductive composite was stretched up to 150% strain (Figure 4b). Patternability and processability were demonstrated by using solution spray coating. A shadow mask with a pattern of parallel lines was fabricated via micromachining and placed on a stretchable fiber mat. Precursor solution (25% (wt/vol) STFA) was then applied with a bottom feed airbrush. Silver nanoparticles were then nucleated to form defined lines with a thickness of 300 mm and a conductivity of 1260 S/cm (Figure 4c).

In summary, we have developed a method to deposit conformal stretchable conductive fiber mats using solution blow spinning and metallic nanoparticle nucleation on non-uniform substrates. The stretchable fiber mats were able to combine electrical conductivity values as high as 2000 S/cm with R/R_0 values as low as 1.13 after 400 cycles of 150% strain. The stable electrical properties of these stretchable conductors potentially stem from robust conductive pathways maintained through silver nanoparticle stabilized fiber-to-fiber contacts. To demonstrate applicability of this method we employed stretchable conductors in simple devices including strain sensors on nitrile gloves and stretchable electrodes connecting LEDs.

Experimental

Stretchable Conductor Fabrication: Solutions of poly(styrene-block-isoprene-block-styrene) (SIS) (Sigma Aldrich, 22 wt% Styrene content) and tetrahydrofuran (THF) (Fisher Scientific, 99.9%) were prepared and fed with a constant feed rate (10 ml/hr) through the nozzle of the solution blow spinning setup (Figure 1b). The air pressure was kept constant during the blow spinning process at 50 psi. Elastomeric fibers were accumulated on a metal mesh. The resulting polymer fiber construct was lifted from the metal mesh and immersed in a previously prepared organometallic solution consisting of silver trifluoroacetate (STFA) (Sigma Aldrich, 98%) and ethanol (Pharmco-Aaper, 99%) for 30 minutes, then dried in a vacuum desiccator. Silver nanoparticle nucleation was initiated via drop-wise addition of reducing solution consisting of hydrazine hydrate (50% (vol/vol)) (Sigma Aldrich, 50%-60%), deionized water (25% (vol/vol)) and ethanol (25% (vol/vol)). The resultant conductive fiber composite was washed thoroughly with water to eliminate any unbound nanoparticles and dried overnight under vacuum.

Characterization: Scanning Electron Microscopy (SEM) (Hitachi SU-70) and Transmission Electron Microscopy (TEM) (JEOL 2100F) were used to characterize the microstructure of the polymer-nanoparticle composites. The TEM sample used for cross-section analysis was prepared using a microtome (Leica EM UC-6). Fiber diameter is reported as an average of 50 measurements taken from three SEM images. A dynamic mechanical analyzer (TA Instruments

Q800) and an Instron tensile tester (model 3345) were used to characterize the mechanical properties of the stretchable conductors. The electrical conductivity of the stretchable conductor samples were measured using a custom built automated 4-point probe measurement system connected to a Keithey 2400 Sourcemeter. The normalized resistance measurements under mechanical strain were performed using a high precision optical stage and an Ohmmeter (Amprobe 33XR-A).

Device Fabrication and Patterning: The glove strain sensors were fabricated via fiber mat deposition on a nitrile glove and subsequent nanoparticle nucleation. Once the glove was completely covered with elastomeric fibers, lines were drawn on each finger using a flow-pen (Paasche F-I/32) filled with STFA solution (25% (wt/vol)). The conductive lines were formed after hydrazine hydrate solution was applied drop wise onto the STFA patterned lines. The strain sensing measurements were performed using an Ohmmeter (Amprobe 33XR-A) attached to the conductive lines on the glove with alligator clips. The conductive composite connecting the LEDs was stretched using a precision optical stage, while being powered with a DC source (Hewlett Packard E3630A) with constant voltage (5V). The parallel lines were patterned on planar elastomeric fiber mats using spray deposition of 25% (wt/vol) STFA solution with a bottom feed airbrush (40 psi air pressure, 20 ml/hr solution feed) through a micromachined shadow mask and subsequently nucleated by spray deposition of hydrazine hydrate solution. The patterned stretchable conductor was washed with water and dried under vacuum overnight prior to characterization.
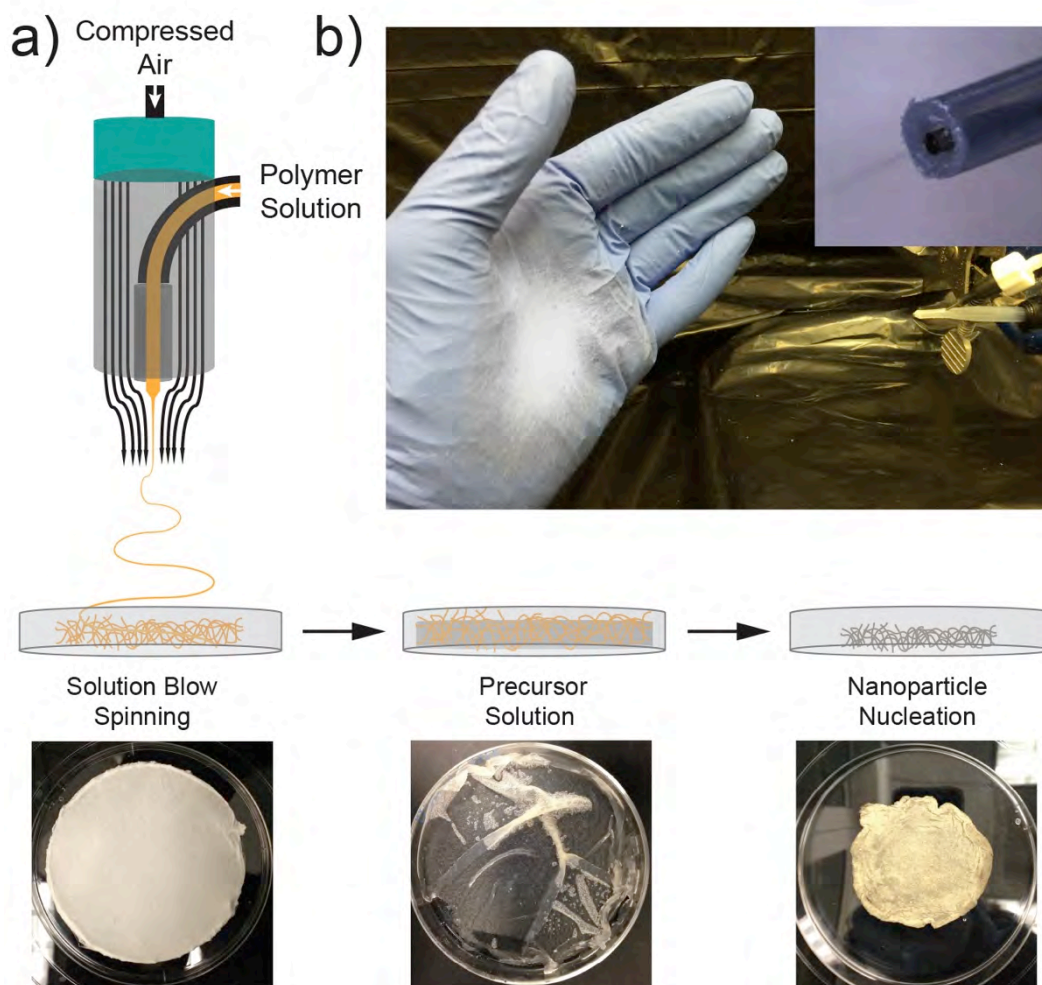
Figure 1. a) Schematic illustration of SIS blow spun fiber network fabrication and images of the as spun fiber network, fiber mat swollen with silver nanoparticle precursor solution, and conductive polymer-nanoparticle composite after nanoparticle nucleation. b) Image of the direct deposition of SIS fibers onto a gloved hand (nozzle used for solution blow spinning-inset).
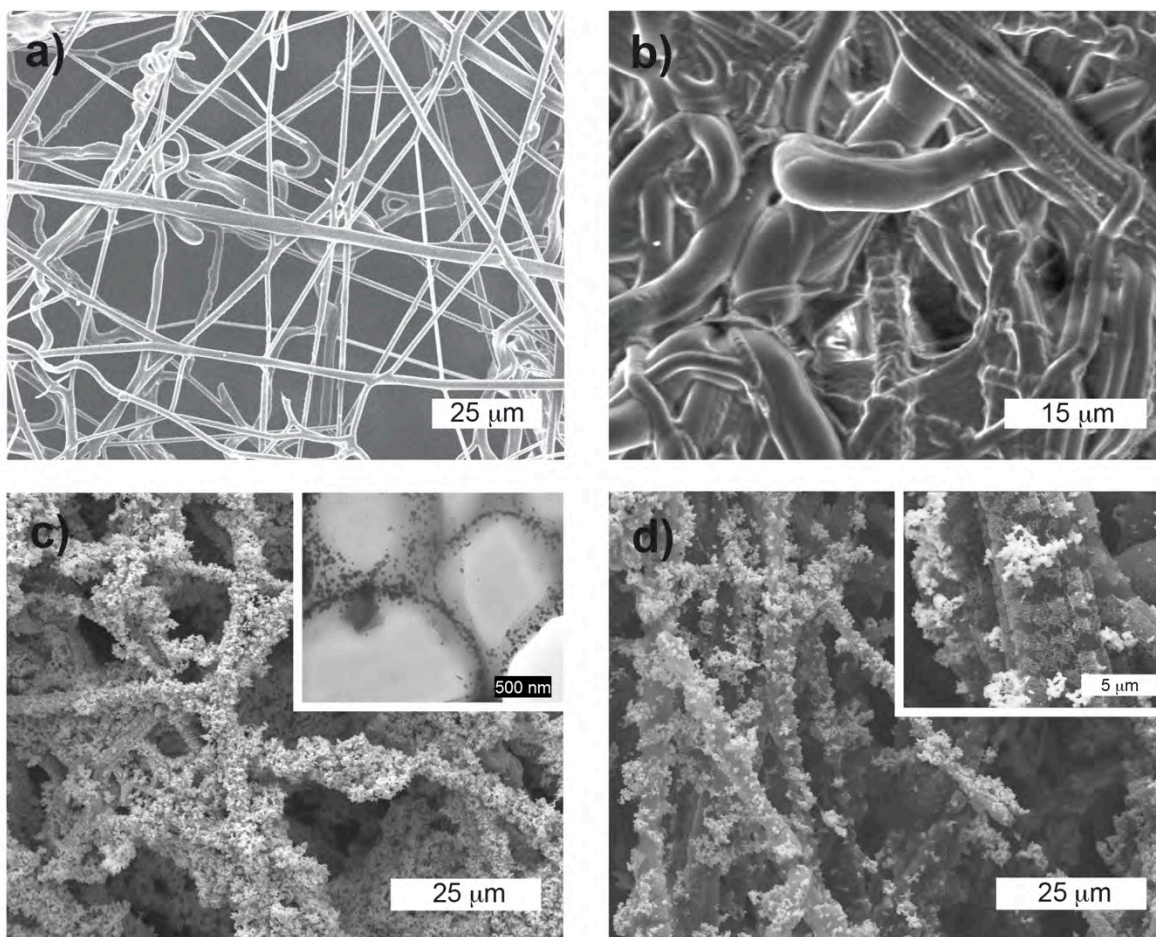
Figure 2. a) SEM images of SIS blow spun fiber network, b) swollen with silver precursor solution, c) conductive composite decorated with silver nanoparticles (Cross-section TEM image of conductive SIS fibers-inset), d) conductive composite stretched to 100% strain (SEM image of a fiber bundle under 100% strain-inset).
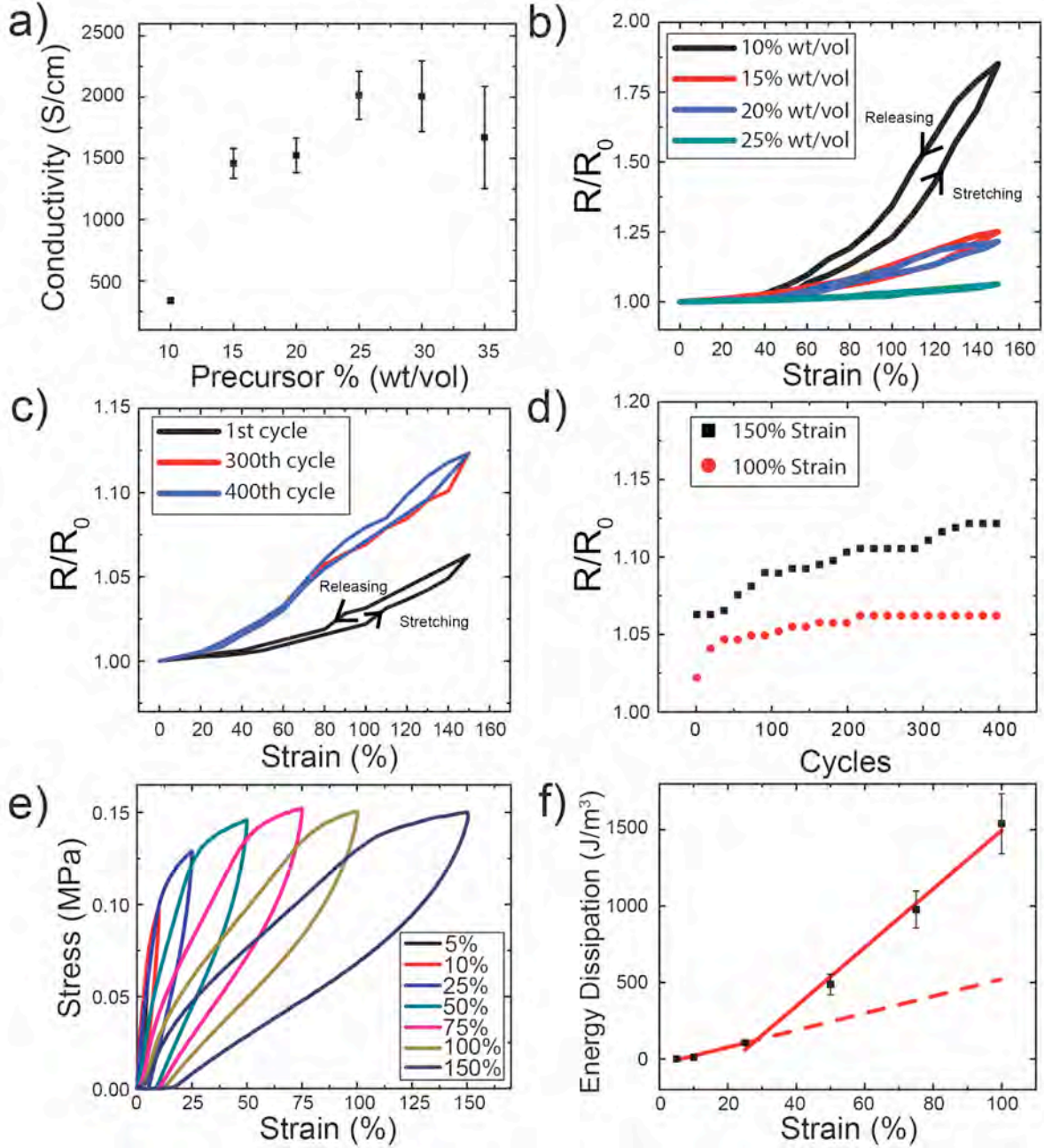
Figure 3. a) Electrical conductivity of stretchable conductors as a function of STFA concentration (n=5). b) Normalized resistance values as a function of uniaxial tensile strain for various STFA concentrations. c,d) Normalized resistance values as a function of uniaxial tensile strain and cycle number, e) stress/strain cycling curves, and f) energy dissipation and corresponding linear fits of stretchable conductors fabricated with 25% (wt/vol) STFA solution (n=3). Error bars represent standard deviation.
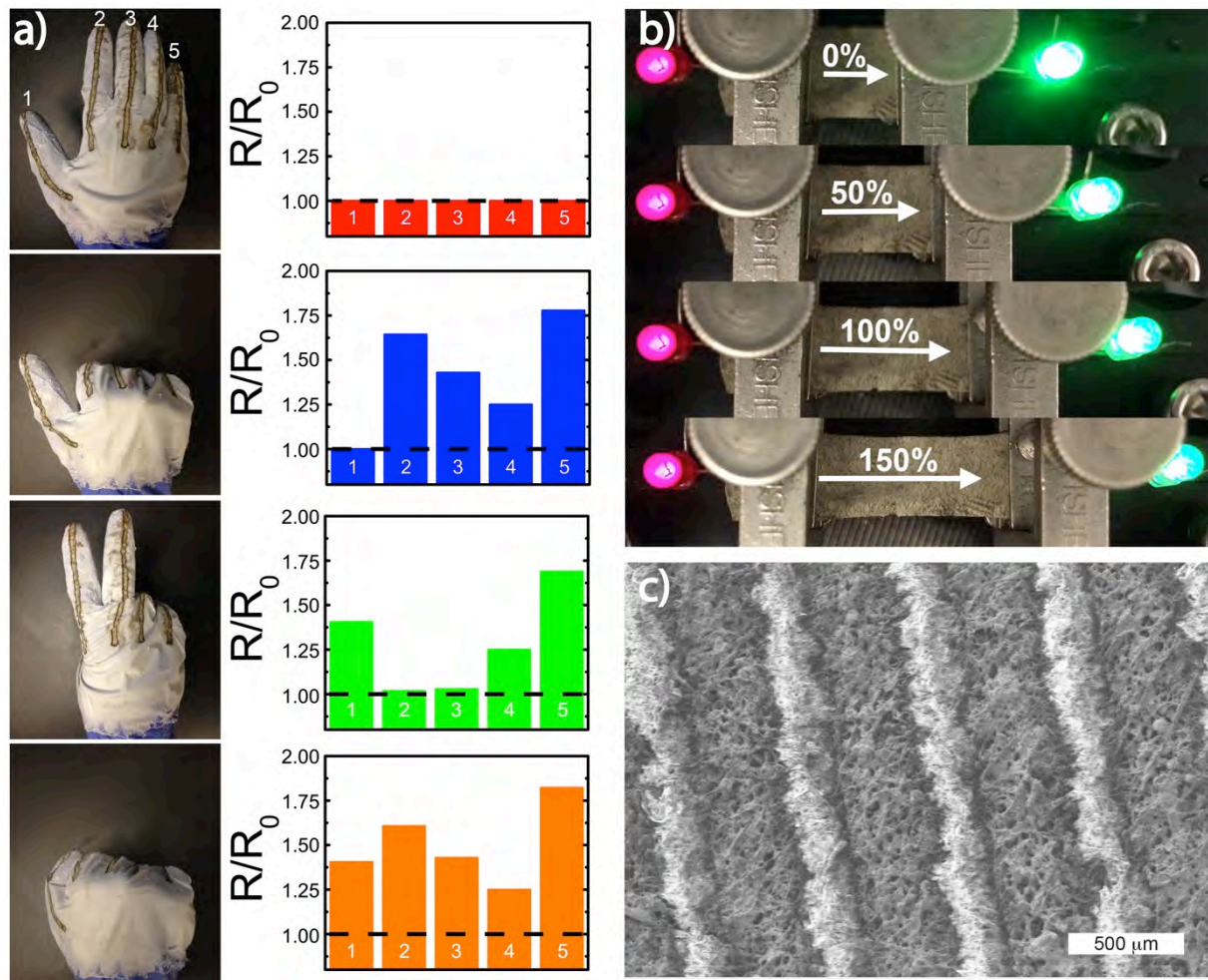
Figure 4. a) Images of hand gestures performed wearing a nitrile glove coated with elastomeric fiber mat and patterned with conductive lines. Normalized resistance values for conductive lines patterned on each finger numbered from 1 to 5. b) Images of LED circuit operating under various strain conditions c) SEM image of parallel conductive lines patterned using spray deposition.
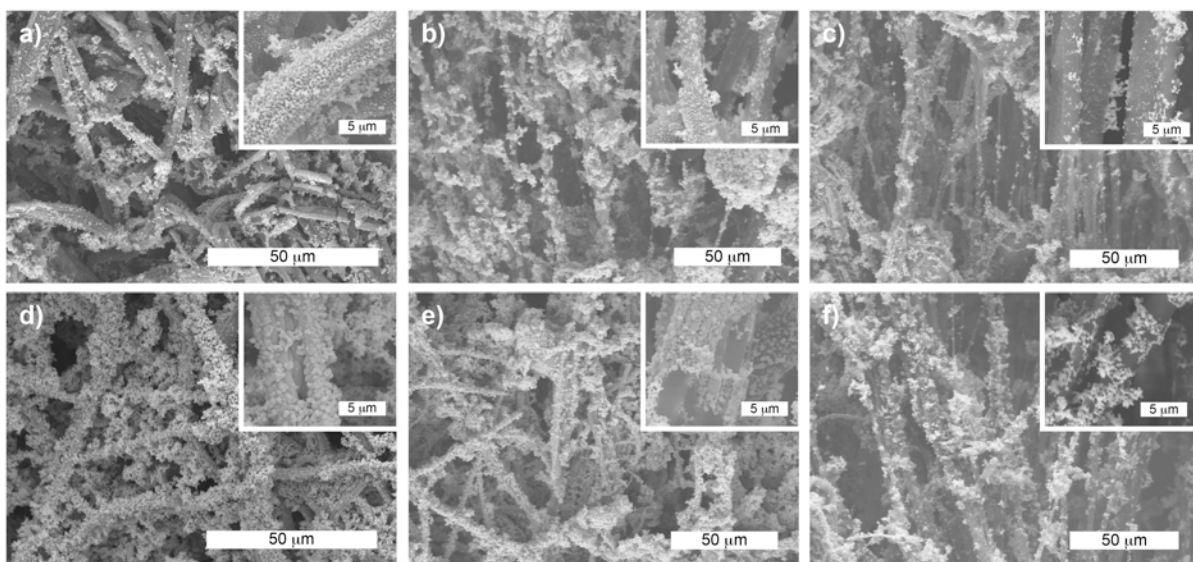
Figure S1. SEM images of conductive composites fabricated using 10% (wt/vol) STFA solutions under a) 0% strain, b) 50% strain, and c) 100% strain. SEM images of conductive composites fabricated using 25% (wt/vol) STFA solutions under a) 0% strain, b) 50% strain, and c) 100% strain. Higher magnification SEM images of individual fibers for respective conductive composites under different strain values are provided in the inset.
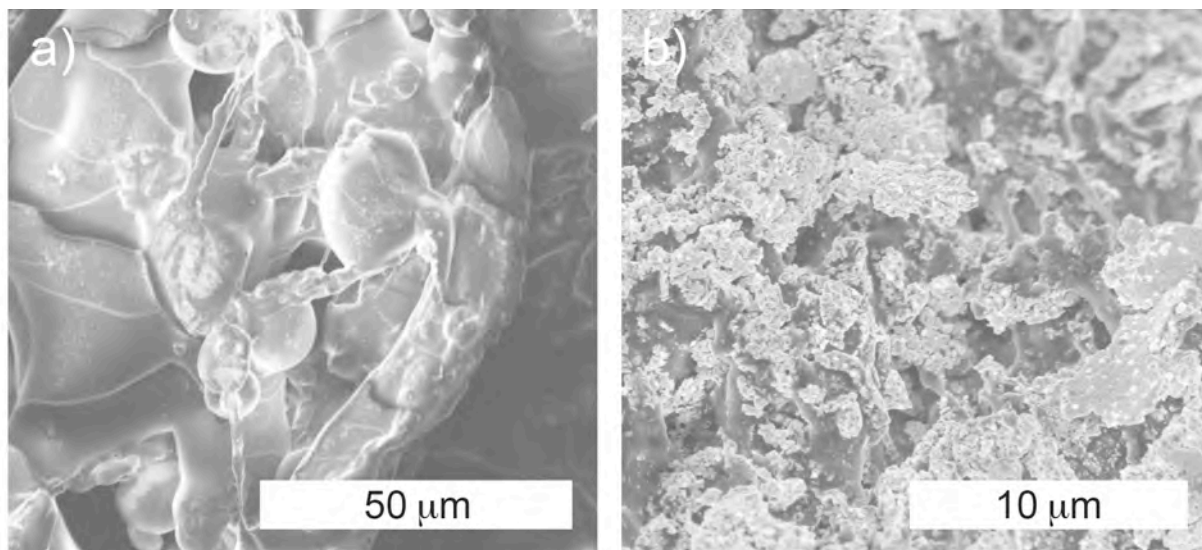

Figure S2. Fiber structure was irreversibly lost during the fabrication process for tri-block copolymers with a styrene weight percentage lower than 22%. a) SEM image of solution blow spun polymer network of low styrene content SIS (14 wt% Styrene) after being swollen with 25% (wt/vol) STFA solution, showing loss of fiber morphology. b) SEM image of the same polymer network after silver nanoparticle nucleation.
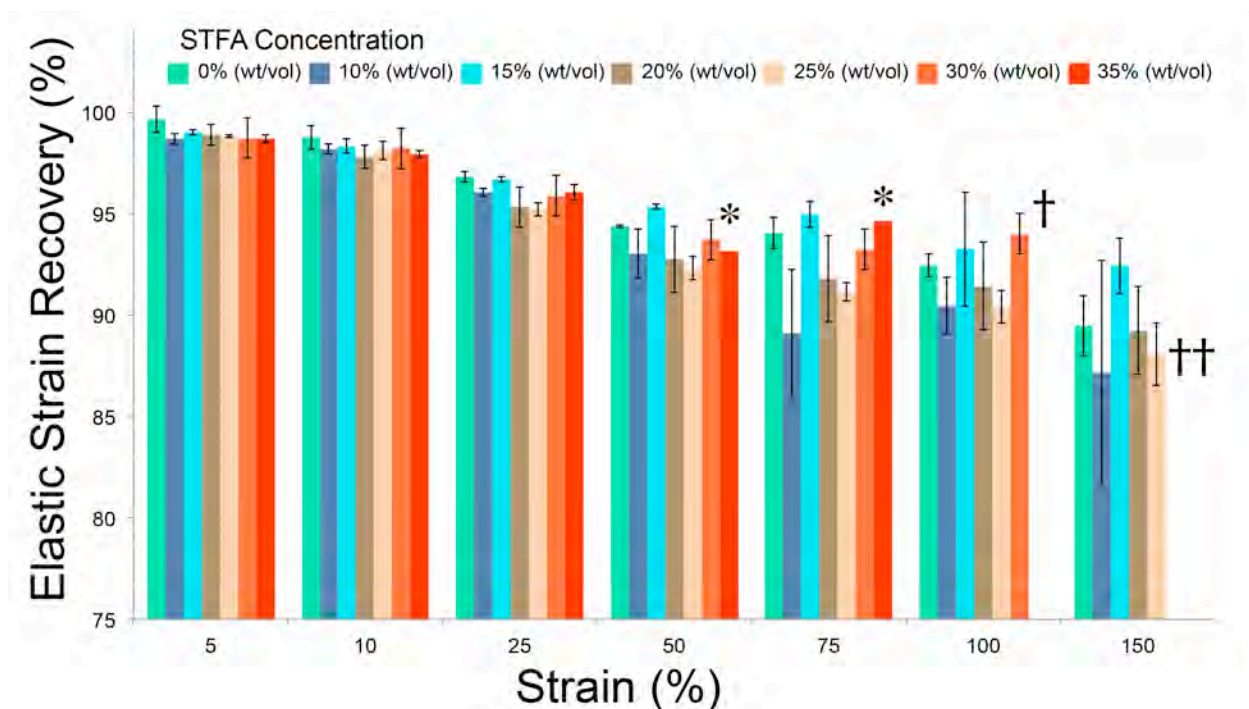
Figure S3. Elastic recovery of SIS fiber mats and stretchable conductors fabricated from different precursor concentrations after consecutive strain cycling to increasing maximum strain values. (*) Indicates that 2 of 3 samples failed during that strain cycle for a specific experimental group. (†) Indicates that all of the samples have failed. Conductive composites fabricated with 25% (wt/vol) STFA solutions have no statistically significant elastic recovery differences relative to an SIS fiber mat control (0% (wt/vol STFA)) after cycling up to 150% strain. (n = 3) for all groups, error bars represent standard deviation.
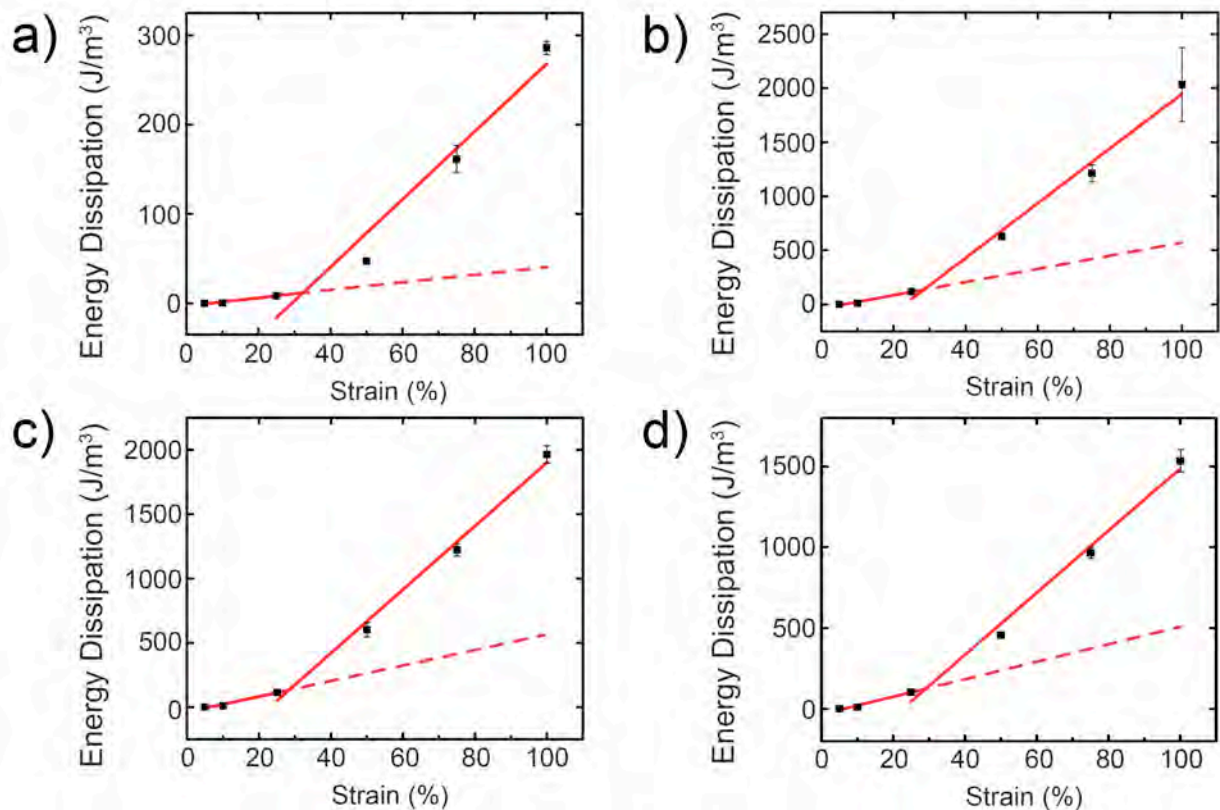
Figure S4. Energy dissipation values of a) elastomeric fiber mats and conductive composites fabricated with b) 10% (wt/vol), c) 15% (wt/vol), d) 20% (wt/vol) STFA solutions as calculated from consecutive strain cycling to increasing maximum strain values. Lines represent linear fits for two discrete regions of dissipative loss behavior originating from unbound and bound fiber contacts. Increased silver content resulted in lower energy dissipation values, possibly due to improved stabilization of bound fiber-to-fiber contacts. (n = 3) for all groups, error bars represent standard deviation.
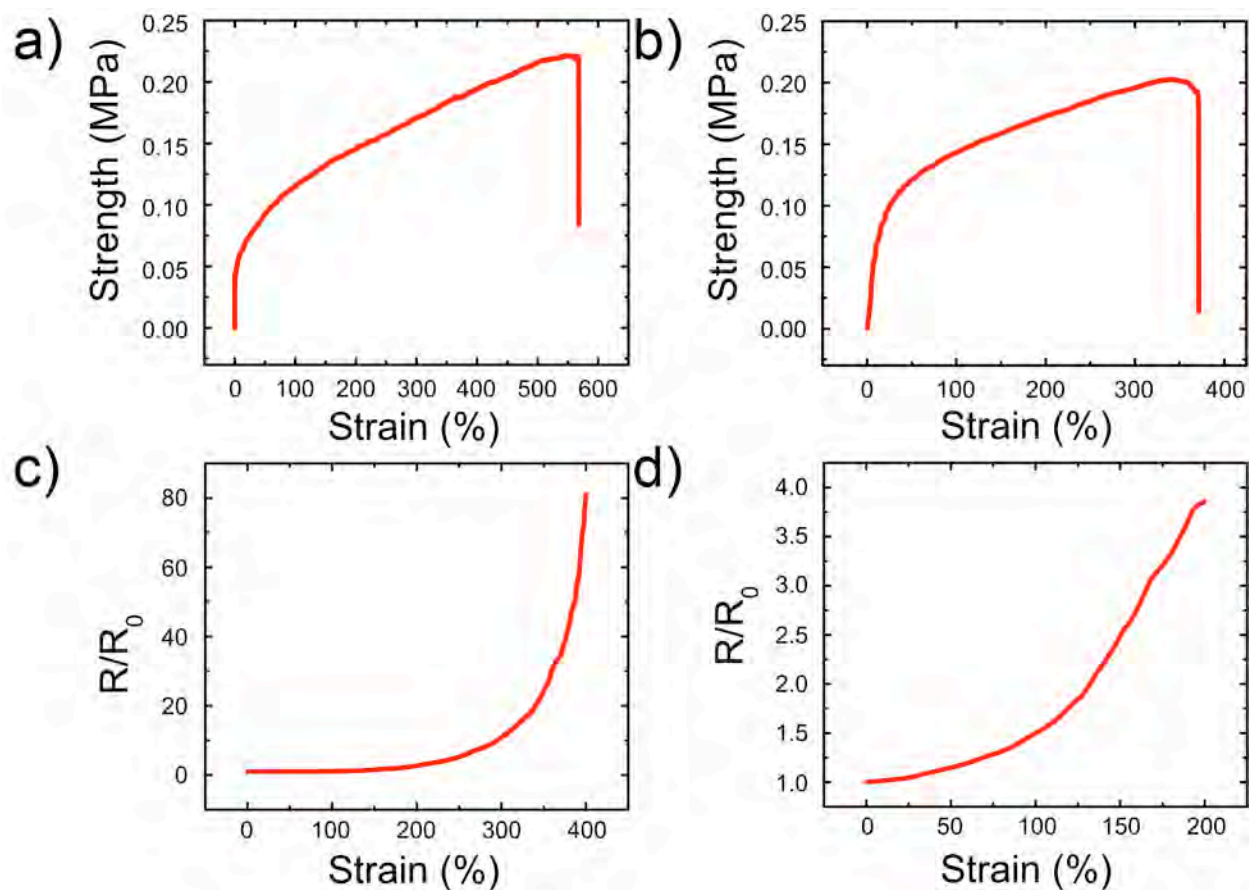
Figure S5. Representative stress/strain curves for a) elastomeric fiber mats, b) conductive composites fabricated with 25% (wt/vol) solutions. Representative normalized resistance values of a) bulk and b) line patterns of conductive composites fabricated with 25% (wt/vol) STFA solutions. The bulk conductors failed between 370% and 400% strain, remaining conductive until mechanical failure.

References

[1]   T. Sekitani, H. Nakajima, H. Maeda, T. Fukushima, T. Aida, K. Hata, T. Someya, Nat Mater 2009, 8, 494.

[2]   D. J. Lipomi, B. C. K. Tee, M. Vosgueritchian, Z. N. Bao, Adv Mater 2011, 23, 1771.

[3]   D. Y. Khang, H. Q. Jiang, Y. Huang, J. A. Rogers, Science 2006, 311, 208.

[4]   M. Kubo, X. F. Li, C. Kim, M. Hashimoto, B. J. Wiley, D. Ham, G. M. Whitesides, Adv Mater 2010, 22, 2749.

[5]   T. Yamada, Y. Hayamizu, Y. Yamamoto, Y. Yomogida, A. Izadi-Najafabadi, D. N. Futaba, K. Hata, Nat Nanotechnol 2011, 6, 296.

[6]   D. J. Lipomi, M. Vosgueritchian, B. C. K. Tee, S. L. Hellstrom, J. A. Lee, C. H. Fox, Z. N. Bao, Nat Nanotechnol 2011, 6, 788.

[7]   J. A. Fan, W. H. Yeo, Y. W. Su, Y. Hattori, W. Lee, S. Y. Jung, Y. H. Zhang, Z. J. Liu, H. Y. Cheng, L. Falgout, M. Bajema, T. Coleman, D. Gregoire, R. J. Larsen, Y. G. Huang, J. A. Rogers, Nat Commun 2014, 5.

[8]   A. H. Najafabadi, A. Tamayol, N. Annabi, M. Ochoa, P. Mostafalu, M. Akbari, M. Nikkhah, R. Rahimi, M. R. Dokmeci, S. Sonkusale, B. Ziaie, A. Khademhosseini, Adv Mater 2014.

[9]   T. Sekitani, T. Someya, Adv Mater 2010, 22, 2228.

[10]   T. Sekitani, Y. Noguchi, K. Hata, T. Fukushima, T. Aida, T. Someya, Science 2008, 321, 1468.

[11]   K. H. Kim, M. Vural, M. F. Islam, Adv Mater 2011, 23, 2865.

[12]   F. Xu, Y. Zhu, Adv Mater 2012, 24, 5117.

[13]   Y. Kim, J. Zhu, B. Yeom, M. Di Prima, X. L. Su, J. G. Kim, S. J. Yoo, C. Uher, N. A. Kotov, Nature 2013, 500, 59.

[14]   M. Park, J. Im, M. Shin, Y. Min, J. Park, H. Cho, S. Park, M. B. Shim, S. Jeon, D. Y. Chung, J. Bae, J. Park, U. Jeong, K. Kim, Nat Nanotechnol 2012, 7, 803.

[15]   J. Park, S. D. Wang, M. Li, C. Ahn, J. K. Hyun, D. S. Kim, D. K. Kim, J. A. Rogers, Y. G. Huang, S. Jeon, Nat Commun 2012, 3; S. Zhu, J. H. So, R. Mays, S. Desai, W. R. Barnes, B. Pourdeyhimi, M. D. Dickey, Adv Funct Mater 2013, 23, 2308.

[16]   N. Bowden, S. Brittain, A. G. Evans, J. W. Hutchinson, G. M. Whitesides, Nature 1998, 393, 146; P. Lee, J. Lee, H. Lee, J. Yeo, S. Hong, K. H. Nam, D. Lee, S. S. Lee, S. H. Ko, Adv Mater 2012, 24, 3326.

[17]   R. S. Guo, Y. Yu, Z. Xie, X. Q. Liu, X. C. Zhou, Y. F. Gao, Z. L. Liu, F. Zhou, Y. Yang, Z. J. Zheng, Adv Mater 2013, 25, 3343.

[18]   K. Y. Chun, Y. Oh, J. Rho, J. H. Ahn, Y. J. Kim, H. R. Choi, S. Baik, Nat Nanotechnol 2010, 5, 853.

[19]   L. B. Hu, M. Pasta, F. La Mantia, L. F. Cui, S. Jeong, H. D. Deshazer, J. W. Choi, S. M. Han, Y. Cui, Nano Lett 2010, 10, 708.

[20]   H. C. Ko, M. P. Stoykovich, J. Z. Song, V. Malyarchuk, W. M. Choi, C. J. Yu, J. B. Geddes, J. L. Xiao, S. D. Wang, Y. G. Huang, J. A. Rogers, Nature 2008, 454, 748; D. H. Kim, Y. S. Kim, J. Wu, Z. J. Liu, J. Z. Song, H. S. Kim, Y. G. Y. Huang, K. C. Hwang, J. A. Rogers, Adv Mater 2009, 21, 3703; D. H. Kim, J. L. Xiao, J. Z. Song, Y. G. Huang, J. A. Rogers, Adv Mater 2010, 22, 2108; M. Kaltenbrunner, T. Sekitani, J. Reeder, T. Yokota, K. Kuribara, T. Tokuhara, M. Drack, R. Schwodiauer, I. Graz, S. Bauer-Gogonea, S. Bauer, T. Someya, Nature 2013, 499, 458.

[21]   B. Y. Ahn, E. B. Duoss, M. J. Motala, X. Y. Guo, S. I. Park, Y. J. Xiong, J. Yoon, R. G. Nuzzo, J. A. Rogers, J. A. Lewis, Science 2009, 323, 1590; J. T. Kim, J. Pyo, J. Rho, J. H. Ahn, J. H. Je, G. Margaritondo, Acs Macro Lett 2012, 1, 375; S. Chung, J. Lee, H. Song, S. Kim, J. Jeong, Y. Hong, Appl Phys Lett 2011, 98.

[22]   G. A. Salvatore, N. Munzenrieder, T. Kinkeldei, L. Petti, C. Zysset, I. Strebel, L. Buthe, G. Troster, Nat Commun 2014, 5.

[23]   E. S. Medeiros, G. M. Glenn, A. P. Klamczynski, W. J. Orts, L. H. C. Mattoso, J Appl Polym Sci 2009, 113, 2322; W. Tutak, S. Sarkar, S. Lin-Gibson, T. M. Farooque, G. Jyotsnendu, D. B. Wang, J. Kohn, D. Bolikal, C. G. Simon, Biomaterials 2013, 34, 2389; A. M. Behrens, B. J. Casey, M. J. Sikorski, K. L. Wu, W. Tutak, A. D. Sandler, P. Kofinas, ACS Macro Letters 2014, 3, 249.

[24]   G. D. Moon, G. H. Lim, J. H. Song, M. Shin, T. Yu, B. Lim, U. Jeong, Adv Mater 2013, 25, 2707.

[25]   K. Lee, B. Lee, C. Kim, H. Kim, K. Kim, C. Nah, Macromol Res 2005, 13, 441.